

POLARIZATION COHERENCE TOMOGRAPHY (PCT): A TUTORIAL INTRODUCTION

By

Shane R Cloude
AEL Consultants
26 Westfield Avenue
Cupar, Fife, Scotland, UK
Tel/fax : +44 1334 650761
e-mail : aelc@mac.com
web : <http://web.mac.com/aelc/>

Polarization Coherence Tomography (PCT):	1
A Tutorial Introduction	1
1.1 Introduction	1
1.2 PCT : Background Theory	3
1.2.1 Relating Radar Interferometry to Radar Polarimetry	3
1.2.2 Range Spectral Filtering and Critical Baseline	6
1.2.3 Volume Decorrelation and Vertical Structure	8
1.2.4 Special Case 1: The Uniform Profile	13
1.2.5 Special Case 2 : The Exponential Profile	14
1.2.6 Generalised Structure Functions	18
1.3 Polarization Coherence Tomography (PCT)	19
1.3.1 First Order Coherence Model	19
1.3.2 Second Order Legendre Model	24
1.4 Parameter Estimation for PCT	28
1.4.1 Surface Phase ϕ_0 Estimation	29
1.4.2 Height Estimation Algorithms for PCT	33
1.4.3 Inclusion of temporal and SNR decorrelation effects in PCT	37
1.5 Summary Algorithm for Polarization Coherence Tomography (PCT)	39
1.6 Case Study : PCT from L-band POLInSAR Simulations	41
1.6.1 Estimation of the Legendre Spectrum for arbitrary polarization w	45
1.6.2 3-D Imaging Results	49
1.7 Conclusions	54
1.8 References	55

1.1 Introduction

Information about vertical structure (i.e. the variation of scattering in the vertical or z-direction) can be considered the missing component in synthetic aperture radar imagery (SAR). SAR is inherently a two-dimensional imaging process, with along-track or azimuth resolution given by one half the real antenna size and slant range resolution determined by the inverse of transmitted bandwidth. However the radar

cross-section observed for a given pixel is the sum or integral of contributions from all scatterers at the same range, encompassing all heights. Hence information about vertical structure is lost. To recover such information we need to image in the 3rd dimension. This chapter is concerned with a new method for doing this, called polarization coherence tomography or PCT.

There are two classes of method proposed in the literature for imaging vertical structure, namely multi-baseline model based inversion [1,2,3,4,5] and radar tomography [6,7,8]. The latter is based on the same principle as synthetic aperture radar itself, namely to synthesise an aperture, but this time in the vertical dimension, and use this to reconstruct a 3-D image. However to do this requires filling a vertical aperture with a large number of sample measurement points. This usually involves collecting data for a relatively large number of parallel flight tracks closely separated in the vertical direction, followed by high-resolution spectral analysis to resolve structure. However, sampling density and irregularity issues usually make this a challenging task and the choice of processing calls for some finesse, the resultant images usually being of much lower resolution than those obtained from conventional SAR processing.

This approach stands in contrast to the first method, based on constructing invertible scattering models for the random media itself. In this approach the vector of observed interferometric coherences for several baselines is constrained by a physical model of the scattering by different vertical profiles and the ‘most-likely’ profile selected to correspond to the observed vector of coherences. This second approach has the advantage of reducing the number of tracks or baselines required but the disadvantage of being susceptible to violations of the underlying model and also non-uniqueness i.e. many different vertical profiles of scattering may yield the same or very similar (i.e. the same within some experimental uncertainty) coherence vectors. For example, the approach in [1,2,3] uses the well known random-volume-over-ground or ‘RVOG’ model to estimate vertical structure but using a Gaussian function expansion in place of the standard exponential [3], which itself arises from the distorted Born model for wave propagation and scattering in a homogeneous layer. In these publications for example it is shown that a range of different structures are usually consistent with the error bounds of the data.

Recently there has emerged a hybrid approach between these two, called polarization coherence tomography or PCT [9,10,11]. In this approach the tomographic or 3-D reconstruction of an arbitrary profile is implemented via a Fourier-Legendre series expansion of the unknown vertical profile followed by estimation of the parameters of this series from interferometric coherence data. Critically, by employing POLInSAR height estimation techniques [12,13,14], this tomographic reconstruction can be linearised and hence implemented efficiently. One key advantage of this approach is that it allows 3-D tomography even with a single baseline pair. In this way it offers a parsimonious or ‘parameter efficient’ approach to 3-D imaging, which is important for any future potential spaceborne applications [15], where multi-baseline acquisitions will always be limited.

In this tutorial we first introduce the basic theory behind PCT and then present a ‘do-it-yourself’ introduction to the processing required using simulated POLInSAR data.

1.2 PCT : Background Theory

1.2.1 Relating Radar Interferometry to Radar Polarimetry

A scattered radar signal may be represented by a complex scalar, representing its amplitude a and phase ϕ as shown in equation 1

$$s_1 = a_1 e^{-i\phi_1} = a_1 e^{-i(k2R_1 + \phi_{s1})} = a_1 e^{-i(\frac{2\pi}{\lambda} 2R_1 + \phi_{s1})} \quad - 1)$$

Here we have further decomposed the phase of the signal into two parts, the first a propagation phase that depends on the distance between the radar and the scattering point (R_1) and the second a scattering phase that depends on the geometry and material of the scatterer. In radar polarimetry we concentrate on looking at the changes of the scattering phase by combining two signals with different polarizations but collected at the same point in space, so cancelling the range phase term as shown in equation 2

$$\left. \begin{aligned} s_1 &= a_1 e^{-i(\frac{4\pi}{\lambda} R_1 + \phi_{s1})} \\ s_2 &= a_2 e^{-i(\frac{4\pi}{\lambda} R_1 + \phi_{s2})} \end{aligned} \right\} \Rightarrow s_1 s_2^* = a_1 a_2 e^{i(\phi_{s2} - \phi_{s1})} \quad - 2)$$

We have seen in other tutorials how to characterize fluctuations in the polarimetric phase due to depolarization in the scattering process by using concepts like entropy etc. In particular we have seen that in the presence of random volume scattering from anisotropic particles in a forest canopy, for example, this depolarization can be very high, leading to a noisy polarimetric phase. It would be useful to be able to counter this depolarization in some way. Radar interferometry provides such an option as we now show.

In radar interferometry we begin again with the reference signal s_1 of equation 1. However rather than diversify polarization for a fixed position, we now keep polarization constant but vary spatial position to collect a second signal s_2 from a new position, separated from the first by a spatial baseline B as shown in figure 1. Note that there are inherently two ways to achieve this. The first, “single pass interferometry”, occurs when we use two radars at the same instant in time to collect signals s_1 and s_2 . Alternatively it is often more convenient (and cost effective) to use a single radar system to collect a signal at position 1 and then move the radar to position 2 at some time later (in a repeat pass satellite orbit for example) to collect s_2 . In the airborne/space radar context this is called “repeat-pass interferometry” and the time difference between the data collections is called the temporal baseline (in seconds), to be contrasted with the spatial baseline B (with units of metres).

Note that we have an additional degree of freedom for ‘single-pass’ sensors in choosing either to transmit and receive from both points (the dual-transmitter mode described in figure 1 and often termed ‘ping-pong’) or just to transmit from 1 and receive on 1 and 2 simultaneously (called the single-transmitter or standard mode). In this case we can avoid the expense and complexity of a second transmitter. However in this case the factor of 4π in equation 1 is halved to 2π , since the phase difference now only depends on $R_1 - R_2$ rather than $2R_1 - 2R_2$. This is equivalent in phase terms

(at least for small baselines) to using half the spatial baseline B in an equivalent ping-pong mode. In what follows we consider the dual transmitter ping-pong mode (which by definition is the mode used in repeat-pass interferometry) to illustrate the main form of the governing equations.

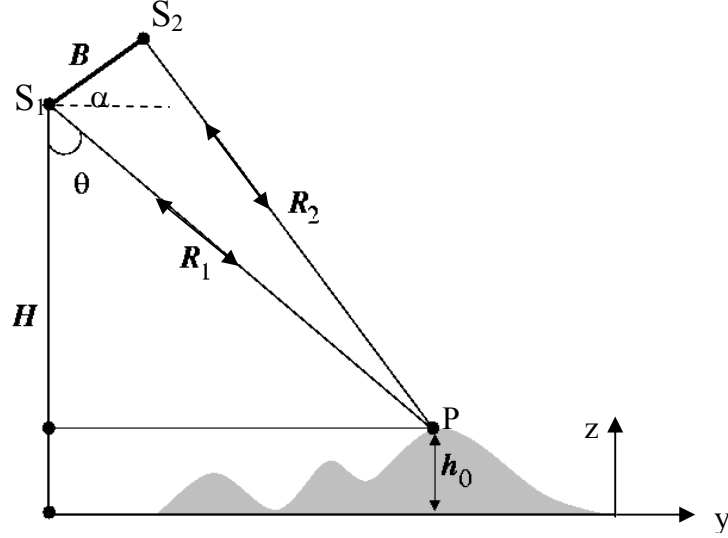


Figure 1: Geometry of Radar Interferometry

In either case, when we form the complex product $s_1 s_2^*$ for interferometry we cancel the scattering phase terms (assuming they are the same, we shall see later how good this approximation is in practice) and keep the geometrical phase. In effect we now obtain a signal phase devoid of wave scattering effects which depends only on the difference in range between the two positions, $\Delta R = R_1 - R_2$ as shown in equation 3

$$\left. \begin{aligned} s_1 &= a_1 e^{-i(\frac{2\pi}{\lambda} 2R_1 + \phi_{s1})} \\ s_2 &= a_2 e^{-i(\frac{2\pi}{\lambda} 2R_2 + \phi_{s2})} \end{aligned} \right\} \Rightarrow s_1 s_2^* = A e^{-i(\frac{4\pi}{\lambda} \Delta R)} \quad - 3)$$

The key radar observable is now the interferometric phase ϕ , as defined in equation 4

$$\phi = \arg \{ s_1 s_2^* \} = -\frac{4\pi}{\lambda} \Delta R + 2\pi N \quad N = 0, \pm 1, \pm 2, \dots \quad - 4)$$

Note that this interferometric phase is 2π ambiguous i.e. for every shift of half a wavelength $\lambda/2$ in range difference ΔR , the phase difference repeats itself

The relationship between ΔR , ϕ and the elevation h_0 of the scatterer can be defined from the geometry of the triangle $S_1 S_2 P$ in figure 1. However we can simplify somewhat this relationship for the case when the angular width of the baseline seen from the point P is small i.e. $B \ll R$. In this case we can obtain a simple linear relationship between phase and height of the form $\phi = k_z h_0$ as we now show. The scale factor k_z is called the interferometric wavenumber. To derive an expression for this scaling factor we first consider construction of a local coordinate system around the point P as shown in figure 2. The y -axis represents the local surface tangent and z

the local vertical. Considering first the y-axis, the extra contribution to phase for a point P separated locally from the origin by distance y is approximately $y \sin \theta$ as shown in figure 2

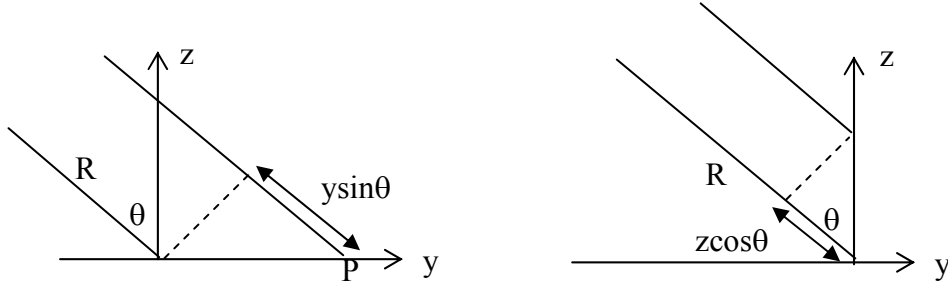


Figure 2: Approximate Ray Path Geometry for Phase Estimation

Using this we can then write the phase for signals scattered from point P at ends 1 and 2 of a baseline as shown in the top line of equation 5

$$\left. \begin{aligned} s_1 &= a_1 e^{-i \frac{4\pi}{\lambda} (R + y \sin \theta_1)} \\ s_2 &= a_2 e^{-i \frac{4\pi}{\lambda} (R + y \sin \theta_2)} \end{aligned} \right\} \Rightarrow s_1 s_2^* = A e^{i \frac{4\pi}{\lambda} (\sin \theta_2 - \sin \theta_1)} \quad - 5)$$

$$s_1 s_2^* = A e^{i \frac{4\pi}{\lambda} y (\sin \theta_2 - \sin \theta_1)} = A e^{i \frac{4\pi}{\lambda} 2y \cos(\frac{\theta_1 + \theta_2}{2}) \sin(\frac{\theta_2 - \theta_1}{2})} \approx A e^{i \frac{4\pi \Delta \theta}{\lambda} y \cos(\theta)}$$

$$s_1 s_2^* = A e^{-i \frac{4\pi}{\lambda} z (\cos \theta_2 - \cos \theta_1)} = A e^{i \frac{4\pi}{\lambda} 2z \sin(\frac{\theta_1 + \theta_2}{2}) \sin(\frac{\theta_2 - \theta_1}{2})} \approx A e^{i \frac{4\pi \Delta \theta}{\lambda} z \sin(\theta)}$$

In case the angular difference to the point $\Delta \theta = (\theta_2 - \theta_1)$ is small (i.e. $B \ll R$) we can further simplify this expression as shown in the second line of equation 5. Similarly, for points P shifted in the z direction (right hand side of figure 2) we have an extra phase term $-z \cos \theta$, which leads to a corresponding interferometric phase as shown in the bottom line of equation 5

Combining these two we obtain the following expression for the interferometric phase as a function of y and z around the point P

$$\phi_{if}(y, z) = \frac{4\pi \Delta \theta}{\lambda} (y \cos \theta + z \sin \theta) \quad - 6)$$

Currently we see that the phase varies not only with height of the point P (the coordinate z) but also for shifts in surface position (y). This disturbs somewhat our desire to have a clean phase-to-height conversion. We can remove this problem and obtain our desired result by shifting the frequency of the signal collected at position 2 *before* forming the interferogram using a process called range spectral filtering as follows.

1.2.2 Range Spectral Filtering and Critical Baseline

To remove the surface (y) phase dependence, for each frequency f in the spectrum of signal 1 we generate an interferogram with a shifted frequency component of signal 2, to yield a phase of the form $\phi = \arg(s_1(f)s_2^*(f + \Delta f))$. In order to completely cancel the y dependence of phase for arbitrary position P, we must employ a shift Δf based on the local geometry as shown in equation 7. As shown, this then removes the y dependence of phase from equation 6 and yields a scale factor k_z equal to the desired vertical sensitivity of the interferometer.

$$\begin{aligned}
 \text{if } \Delta f &= \frac{\Delta \theta}{\tan \theta} f \\
 \Rightarrow \Delta k &= k \frac{2\Delta \theta}{\tan \theta} = \frac{4\pi\Delta \theta}{\lambda \tan \theta} \\
 \Rightarrow \phi &= \phi_{if} + \Delta k(z \cos \theta - y \sin \theta) \\
 \Rightarrow \phi &= \frac{4\pi\Delta \theta}{\lambda} (y \cos \theta + z \sin \theta) + \frac{4\pi\Delta \theta}{\lambda \tan \theta} (z \cos \theta - y \sin \theta) \quad - 7) \\
 \Rightarrow \phi &= \frac{4\pi\Delta \theta}{\lambda \sin \theta} z = \frac{\partial \phi}{\partial z} z = k_z z \\
 \Rightarrow k_z &= \frac{4\pi\Delta \theta}{\lambda \sin \theta} \approx \frac{4\pi B_n}{\lambda R \sin \theta}
 \end{aligned}$$

Before leaving this topic we highlight two important issues.

1) The frequency shift used in equation 7 is actually a function of the *local* angle of incidence at the point P. Hence in the presence of topographic variations it is affected by range slopes. For example, if the terrain is sloped towards the radar then the effective angle of incidence required to determine the frequency shift is reduced. In the extreme case, when the surface slope equals the radar angle of incidence, we end up with effective normal incidence onto the surface and lose sensitivity completely. In this case we obtain so called ‘blind angles’ for the interferometer. Hence in general, in the presence of range slope η , we must modify the expression for spectral shift as shown in equation 8.

$$\Delta f = -\frac{cB_{\perp}}{R_0 \lambda \tan(\theta - \eta)} \quad - 8)$$

As an example, we consider evaluation of the required spectral shift for typical values of a space radar (ERS-1) operating at 23 degrees of incidence at C band ($\lambda = 5.66\text{cm}$) and transmitting a signal with bandwidth 15.5 MHz with a slant range of 840km. Figure 3 shows the required frequency shift as a function of surface slope. We note the following important features:

- a) As slope increases from zero, the frequency shift required eventually exceeds the bandwidth of the pulse ($\Delta f/W = 1$). This is the start of a band of ‘blind angles’ and the width of this band is defined from this point until the slope increases to the extent that the frequency shift comes back into the pulse bandwidth. This high angle range however is plagued by layover distortion in

radar imaging, whereby points at the top of a slope are at closer range to the radar than those at the foot of the slope.

- b) In the negative range slope direction (away from the radar) the required shift slowly decreases to zero for grazing incidence on the surface. Thereafter the slope disappears into shadow and there is no longer a measurable radar backscatter return.

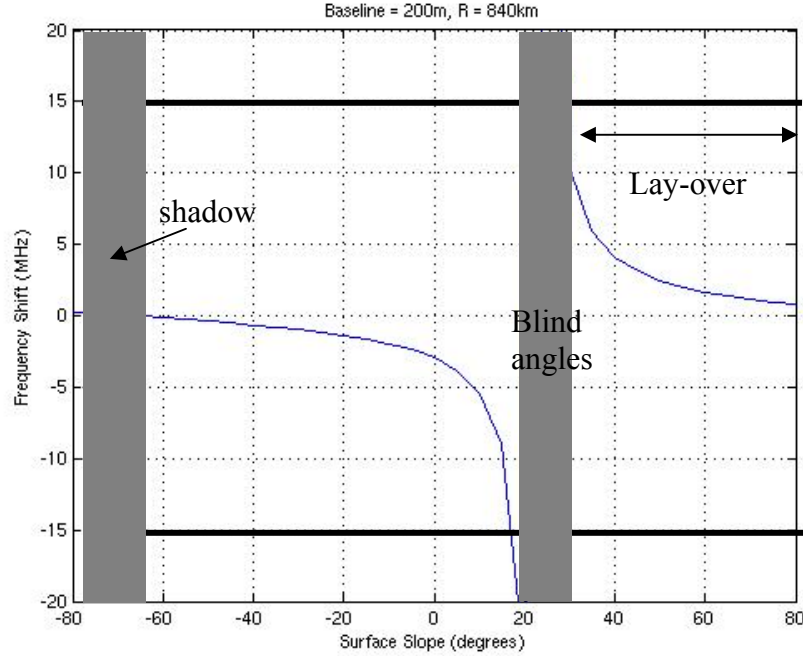


Figure 3: Example of Frequency Shift versus Surface Slope

Hence correct application of the frequency shift concept requires detailed knowledge of the terrain slope. This can be obtained for example if a reference digital elevation model (DEM) is available, from which the range slopes can be calculated by spatial differentiation. In this way an adaptive variation of spectral shift can be performed. In the absence of such topographic information however a compromise shift corresponding to the mean slope can be used, recognising that there will be some errors in the presence of severe topography.

2) Critical Baseline

We see from equation 7 that we can always increase the sensitivity of the interferometer by increasing the normal component of the baseline B_n . However there is a limit to this process, as eventually the frequency shift required will exceed the available bandwidth of the radar signal. If this bandwidth is W Hz, then by equating the shift to W we can obtain an expression for the critical baseline as shown in 9

$$W = -\frac{cB_{\perp,crit}}{R_0\lambda\tan(\theta-\eta)} \Rightarrow B_{\perp,crit} = \left| \frac{WR_0\lambda\tan(\theta-\eta)}{c} \right| \quad - 9)$$

Note also that this frequency shift leads to a reduction in useful bandwidth and hence to a reduction in range resolution of the radar system. This arises because with a shift

there is a reduced common overlap between the spectra at points 1 and 2 as shown schematically in figure 4

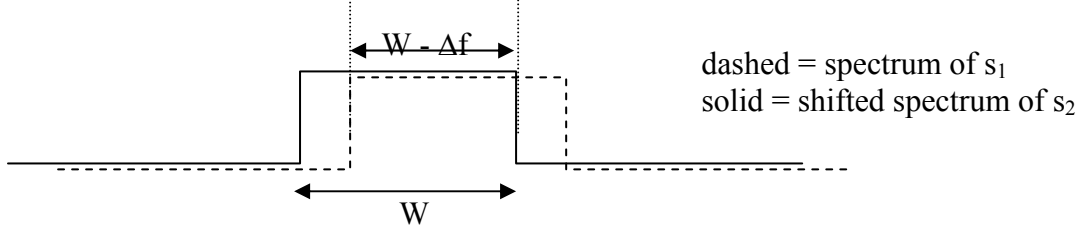


Figure 4 : Schematic Representation of Range Spectral Shift

The slant range resolution of an interferometer then has the modified form shown in equation 10

$$\Delta r = \frac{c}{2(W - \Delta f)} \quad - 10)$$

If this spectral shift is applied then by definition the contributions from both ends of the baseline have the same surface component of wave number and hence the same coherent phase addition for surface scatterers. Hence following spectral filtering the coherence of pure surface scattering equals one and there is zero decorrelation. If this processing is not applied then the level of baseline decorrelation is given by the ratio of shifted spectral overlap to total bandwidth W . This results in the expression for baseline decorrelation shown in equation 11

$$\gamma_B = \frac{B_{crit} - B_{\perp}}{B_{crit}} = 1 - \frac{B_{\perp}}{B_{crit}} = 1 - \frac{cB_{\perp}}{W\lambda R_0 \tan(\theta - \eta)} \quad - 11)$$

This expression can be used to assess the relative importance of baseline decorrelation in the overall system coherence budget for a given bandwidth and operating offset baseline. We now turn to consider another much more important source of decorrelation, namely that due to volume scattering.

1.2.3 Volume Decorrelation and Vertical Structure

We saw from equation 8 that we can always choose a frequency shift Δk to remove the y but not the vertical or z dependence of interferometric phase. This is not a problem for bare surfaces, when the scatterers are all localised on a plane at the same height h_0 . However in case there is a vertical distribution of scatterers the situation changes and we encounter a stochastic effects known as volume decorrelation which is connected to vertical structure as we now discuss.

If we have a general continuous variation of scattered power with z given by a vertical structure function $f(z)$, the lower bound of which is at $z = z_0$ and the upper bound of which is at $z = z_0 + h_v$, where h_v is the height of the layer at point P , then the interferometer will see a composite complex signal given by the weighted sum of contributions (taking into account their phase) as shown in equation 12

$$\langle s_1 s_2^* \rangle = \int_{z_o}^{z_o+h_v} f(z) e^{ik_z z} dz \xrightarrow{z'=z-z_o} e^{ik_z z_o} \int_0^h f(z') e^{ik_z z'} dz' \quad - 12)$$

From this we can obtain an expression for the interferometric coherence as the normalised coherent sum of all contributions as shown in equation 13

$$\tilde{\gamma} = \frac{\langle s_1 s_2^* \rangle}{\sqrt{\langle s_1 s_1^* \rangle \langle s_2 s_2^* \rangle}} = e^{ik_z z_o} \frac{\int_0^h f(z') e^{ik_z z'} dz'}{\int_0^h f(z') dz'} = e^{ik_z z_o} |\tilde{\gamma}| e^{i \arg(\tilde{\gamma})} \quad 0 \leq |\tilde{\gamma}| \leq 1 \quad - 13)$$

This in general will have an amplitude less than 1, which then corresponds to an increase in the local variance of the interferometric phase around a pixel. Hence the deterministic integral in equation 13 tells us something about the stochastic properties of the phase. In the limit, 13 can have an amplitude equal to zero (when the numerator sums to zero) at which point the phase becomes noise-like, with a uniform probability distribution between 0 and 2π . In general however it will lie somewhere between 0 and 1 and in fact, unlike in polarimetry, we have some control over the coherence because we can control k_z in the numerator by selecting an appropriate baseline B.

Note that equation 13 is a complex coherence i.e. it has mean phase as well as magnitude and part of the phase arises from the integral of the structure function shown in the numerator. This shows that there is indeed a direct relationship between the observed complex coherence and important structural properties of the scattering layer. For example, the height of the layer is found in the limits of the integral, the phase of the surface, while not equal to the phase of the coherence, is a multiplying scale factor and finally the vertical structure function $f(z)$ influences the coherence in both amplitude and phase. Special cases of the structure function are often assumed in practice, for example, the simplest, a constant scattering amplitude with depth, or an exponential to more accurately model wave extinction effects in the layer. Here we first develop a general theory of volume decorrelation based on arbitrary structure functions and then specialise our discussion to these important special cases. The approach we use is to expand the bounded function $f(z)$ in a Fourier-Legendre series as follows. We first normalize the range of the integral in the numerator by a change of variable as shown in 14

$$\int_0^h f(z') e^{ik_z z'} dz' \xrightarrow{z_L = \frac{2z'}{h_v} - 1} \int_{-1}^1 f(z_L) e^{ik_z z_L} dz_L \quad - 14)$$

We then rescale variation of the real non-negative function $f(z)$ so that if $0 \leq f(z) \leq \infty$ then $f(z_L) = f(z) - 1$ and $-1 \leq f(z_L) \leq \infty$. Critically we can now develop $f(z_L)$ in a Fourier-Legendre series on $[-1,1]$ as shown in equation 15

$$f(z_L) = \sum_n a_n P_n(z_L) \quad - 15)$$

$$a_n = \frac{2n+1}{2} \int_{-1}^1 f(z_L) P_n(z_L) dz'$$

where the first few Legendre Polynomials of interest to us are given explicitly as shown in equation 16

$$\begin{aligned}
P_0(z) &= 1 \\
P_1(z) &= z \\
P_2(z) &= \frac{1}{2}(3z^2 - 1) \\
P_3(z) &= \frac{1}{2}(5z^3 - 3z) \\
P_4(z) &= \frac{1}{8}(35z^4 - 30z^2 + 3) \\
P_5(z) &= \frac{1}{8}(63z^5 - 70z^3 + 15z) \\
P_6(z) &= \frac{1}{16}(231z^6 - 315z^4 + 105z^2 - 5)
\end{aligned} \tag{16}$$

Figure 5 shows plots of these functions for $h_v = 10\text{m}$. The first represents a simple uniform distribution, while the second includes linear variation followed by quadratic etc. with the higher order functions offering ever-higher resolution of functional variation. In this way any function can be represented over the interval from $z = 0$ to $z = h_v$ by a Legendre spectrum or set of coefficients a_n , calculated by the integrals shown in equation 15. The numerator and denominator of the general expression for coherence can now be written as shown in equation 17

$$\begin{aligned}
\int_0^{h_v} f(z') e^{ik_z z'} dz' &= \frac{h_v}{2} e^{i \frac{k_z h_v}{2}} \int_{-1}^1 (1 + f(z_L)) e^{i \frac{k_z h_v}{2} z_L} dz_L \\
\int_0^{h_v} f(z) dz &= \frac{h_v}{2} \int_{-1}^1 (1 + f(z_L)) dz_L
\end{aligned} \tag{17}$$

from which it follows finally that the coherence can be written in terms of the Legendre series as shown in equation 18

$$\begin{aligned}
\tilde{\gamma} &= e^{ik_z z_0} e^{i \frac{k_z h_v}{2}} \frac{\int_{-1}^1 (1 + f(z_L)) e^{i \frac{k_z h_v}{2} z_L} dz_L}{\int_{-1}^1 (1 + f(z_L)) dz_L} \\
&= e^{ik_z z_0} e^{ik_v} \frac{\int_{-1}^1 (1 + \sum_n a_n P_n(z_L)) e^{ik_v z_L} dz_L}{\int_{-1}^1 (1 + \sum_n a_n P_n(z_L)) dz_L}
\end{aligned} \tag{18}$$

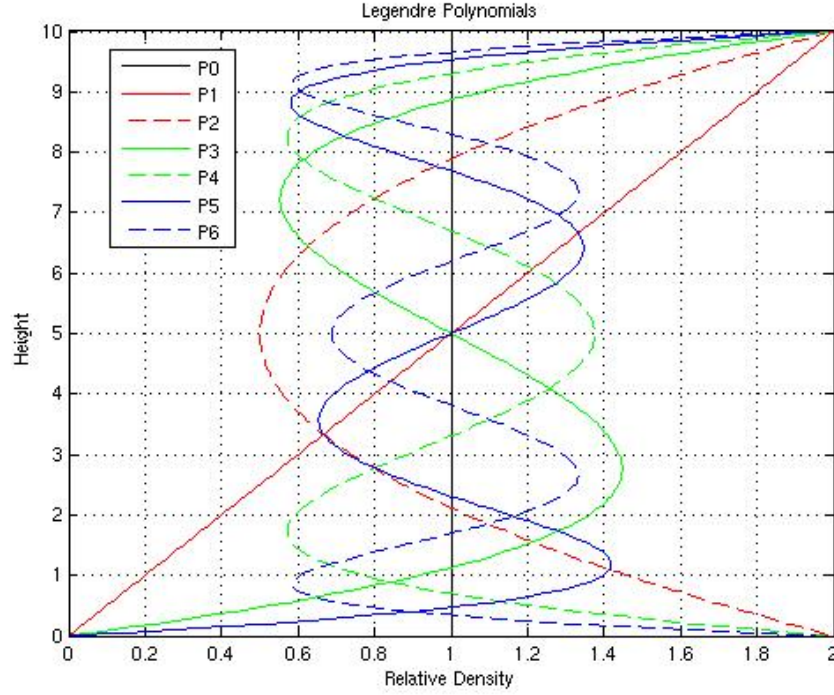


Figure 5: The Legendre Polynomials evaluated for 10m high Volume

By expanding the series and collecting terms, this equation can be rewritten in simplified form as shown in equation 19

$$\begin{aligned}
 \tilde{\gamma} &= e^{ik_z z_0} e^{ik_v} \frac{(1+a_0) \int_{-1}^1 e^{ik_v z_L} dz_L + a_1 \int_{-1}^1 P_1(z_L) e^{ik_v z_L} dz_L + a_2 \int_{-1}^1 P_2(z_L) e^{ik_v z_L} dz_L + \dots}{(1+a_0) \int_{-1}^1 dz_L + a_1 \int_{-1}^1 P_1(z_L) dz_L + a_2 \int_{-1}^1 P_2(z_L) dz_L + \dots} \\
 &= e^{ik_z z_0} e^{ik_v} \frac{(1+a_0)f_0 + a_1 f_1 + a_2 f_2 + \dots a_n f_n}{(1+a_0)} \quad - 19) \\
 &= e^{ik_z z_0} e^{ik_v} (f_0 + a_{10} f_1 + a_{20} f_2 + \dots) \quad a_{i0} = \frac{a_i}{1+a_0}
 \end{aligned}$$

Note that evaluation of the denominator is simplified by using the orthogonality property of the Legendre polynomials. Evaluation of the numerator involves determination of the functions f_n , which employs repeated use of the following identity

$$\int z^n e^{\beta z} dz = \frac{e^{\beta z}}{\beta} (z^n - \frac{n z^{n-1}}{\beta} + \frac{n(n-1) z^{n-2}}{\beta^2} \dots \frac{(-1)^n n!}{\beta^n}) \quad - 20)$$

As an example we show in equation 21 detailed calculation of the first two terms in the series. The first, corresponding to the zeroth order Legendre polynomial just yields a SINC function, while the first order linear polynomial gives a slightly more complicated function. We note that these integrals are all a function of just one parameter, the normalised baseline/height product k_v .

$$\begin{aligned}
f_0 &= \frac{1}{2} \int_{-1}^1 e^{ik_v z} dz = \left[\frac{e^{ik_v z}}{ik_v} \right]_{-1}^1 = \frac{1}{i2k_v} (e^{ik_v} - e^{-ik_v}) = \frac{\sin k_v}{k_v} \\
f_1 &= \frac{1}{2} \int_{-1}^1 z e^{ik_v z} dz = \left[\frac{e^{ik_v z}}{ik_v} \left(z - \frac{1}{ik_v} \right) \right]_{-1}^1 \\
&= \frac{1}{ik_v} (e^{ik_v} + e^{-ik_v}) - \frac{1}{(ik_v)^2} (e^{ik_v} - e^{-ik_v}) \\
&= i \left(\frac{\sin k_v}{k_v^2} - \frac{\cos k_v}{k_v} \right)
\end{aligned} \tag{21}$$

For reference, we give the explicit form of these functions up to 6th order in equation 22. We note the following two important points:

- 1) The even index functions (0,2,4, etc) are real while the odd (1,3,5, etc) are pure imaginary. We note also that the unknown coefficients a_n are always real.
- 2) The functions depend only on the single parameter k_v , itself defined from the product of height h_v and the interferometric wavenumber k_z .

$$\begin{aligned}
f_0 &= \frac{\sin k_v}{k_v} \\
f_1 &= i \left(\frac{\sin k_v}{k_v^2} - \frac{\cos k_v}{k_v} \right) \\
f_2 &= \frac{3 \cos k_v}{k_v^2} - \left(\frac{6 - 3k_v^2}{2k_v^3} + \frac{1}{2k_v} \right) \sin k_v \\
f_3 &= i \left(\left(\frac{30 - 5k_v^2}{2k_v^3} + \frac{3}{2k_v} \right) \cos k_v - \left(\frac{30 - 15k_v^2}{2k_v^4} + \frac{3}{2k_v^2} \right) \sin k_v \right) \\
f_4 &= \left(\frac{35(k_v^2 - 6)}{2k_v^4} - \frac{15}{2k_v^2} \right) \cos k_v + \left(\frac{35(k_v^4 - 12k_v^2 + 24)}{8k_v^5} + \frac{30(2 - k_v^2)}{8k_v^3} + \frac{3}{8k_v} \right) \sin k_v \\
f_5 &= i \left(\frac{-2k_v^4 + 210k_v^2 - 1890}{k_v^5} \cos k_v + \frac{30k_v^4 - 840k_v^2 + 1890}{k_v^6} \sin k_v \right) \\
f_6 &= \left(\frac{42k_v^4 - 2520k_v^2 + 20790}{k_v^6} \right) \cos k_v + \left(\frac{2k_v^6 - 420k_v^4 + 9450k_v^2 - 20790}{k_v^7} \right) \sin k_v
\end{aligned} \tag{22}$$

Graphs of these functions are shown in figure 6. We see that the first is a ‘SINC’ relation between coherence and increasing height-baseline product. This is the expected functional relationship for scattering by the simplest possible structure, a uniform layer.

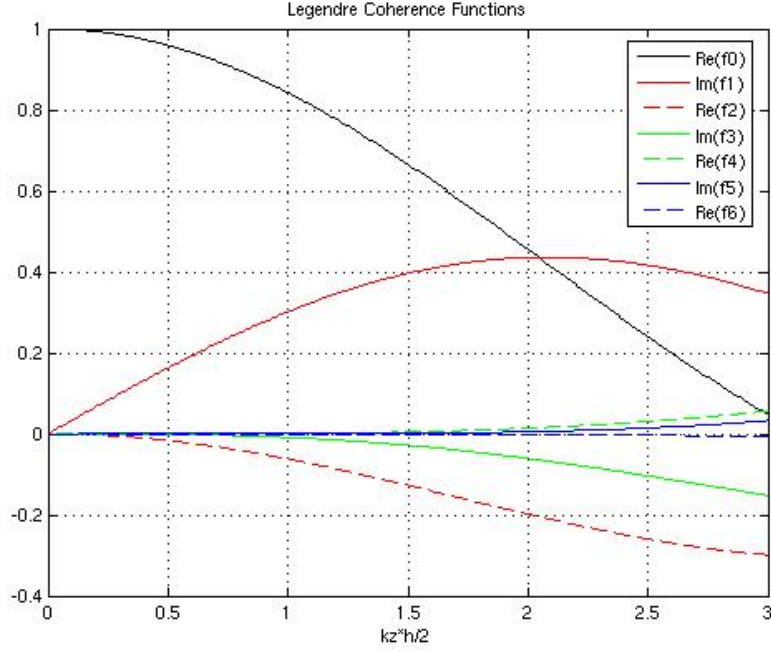


Figure 6: Coherence Basis Functions for Legendre Expansion

However, we see that as the height-baseline product increases, so the other functions become more important. We conclude that, as long as the baseline is large enough, the interferometric coherence is sensitive to variations in structure function $f(z)$. This opens the possibility of inverting this relationship and using measurement of coherence to estimate parameters of the structure function itself.

Before considering such an inversion, there are two special cases of structure function of particular importance due to their widespread use in the literature. We now turn to consider these in more detail:

1.2.4 Special Case 1: The Uniform Profile

If we assume $f(z) = 1$, i.e. a constant structure function, then all the higher order Legendre coefficients are zero and the coherence is given by a complex SINC function as shown in equation 23

$$\tilde{\gamma} = e^{ik_z z_0} e^{ik_z \frac{h_v}{2}} \frac{\sin\left(\frac{k_z h_v}{2}\right)}{\frac{k_z h_v}{2}} \quad - 23)$$

There are two important features of this model. Firstly it shows that volume scattering provides a phase offset from the surface position (z_0), given in this case by half the volume height. Hence in the presence of volume scattering the interferometric phase ϕ no longer represents the true surface position but is offset by a bias. For land surfaces this is called vegetation bias and provides an error source in the use of radar

interferometry for true surface topography mapping. We see that the only way to minimise this effect is to employ small baselines so that the product $k_z h_v$ remains small. However this reduces the sensitivity of the interferometer and is difficult to sustain over forested terrain, where h_v can reach up to 40m or more. Note on the other hand that we cannot simply use the phase of the interferogram to estimate volume height h_v , since the total phase involves addition of an unknown phase shift due to the lower bound of the volume (z_0). Only if we can provide an estimate of this lower bound can we then use the phase to estimate height.

The second key feature of the SINC model is that the coherence amplitude falls with increasing height and hence the phase variance increases with h_v . Note that there is no effect of the lower bounding surface on coherence amplitude (assuming range spectral filtering has been employed) and hence in principle we can use an estimate of measured coherence amplitude to estimate height (for a known baseline). In particular, for short baselines we can expand the SINC function in a series and obtain a useful direct height estimate from coherence amplitude as shown in equation 24

$$x \ll 1 \Rightarrow \frac{\sin x}{x} \approx 1 - \frac{x^2}{6} \Rightarrow h_v \approx \sqrt{\frac{24(1-|\tilde{\gamma}|)}{k_z^2}} \quad - 24)$$

However, as we shall see in the next section, this approach is sensitive to variations in the actual structure function of the volume. The SINC model is really only valid for very small baseline-height products and for most offset baselines higher order terms in the Legendre expansion of $f(z)$ can no longer be ignored. In fact as we shall see, we can turn this idea around and design offset baselines to enhance the higher order terms and hence enable parameter estimation.

Nonetheless, this SINC model is commonly used by radar system designers who wish only to assess the relative importance of volume decorrelation in the overall coherence budget for an interferometer design. Finally we note that this model contains no polarization dependence at all. The volume decorrelation and phase bias of the SINC model are functions only of the height h_v . We shall see however that the higher order terms of the Legendre expansion are sensitive to changes in the wave polarization and this will suggest application of polarimetric interferometry for parameter estimation.

1.2.5 Special Case 2 : The Exponential Profile

A second important structure function is the exponential, widely used to model the physical effects of wave propagation through a volume scattering layer. According to this idea, contributions from the top of the volume are weighted more strongly in the coherence calculation than those deeper into the volume, as the latter experience a smaller incident signal due to wave extinction, combining the physical effects of wave attenuation due to absorption of energy by the volume and scattering loss due to the presence of particles or other inhomogeneities. The combined effect of these two processes can be represented by a one-way power loss extinction coefficient κ_e , with natural units of Nepers/m, but often expressed in engineering units of decibels per meter (dB/m) (where the two systems can be related using equation 25). In addition we note that in radar applications there is a 2-way propagation channel and so the

signal is attenuated both on the way in and out of the volume (see figure 7). Hence the total extinction is $2\kappa_e$. Finally we must also account for the increased attenuation path length through the medium when illuminated at angle of incidence θ_0 as shown in figure 7.

$$\kappa_e^{dB} = \frac{10\kappa_e}{\ln(10)} \approx 4.34\kappa_e \Rightarrow \kappa_e \approx 0.057\kappa_e^{dB} \quad - 25)$$

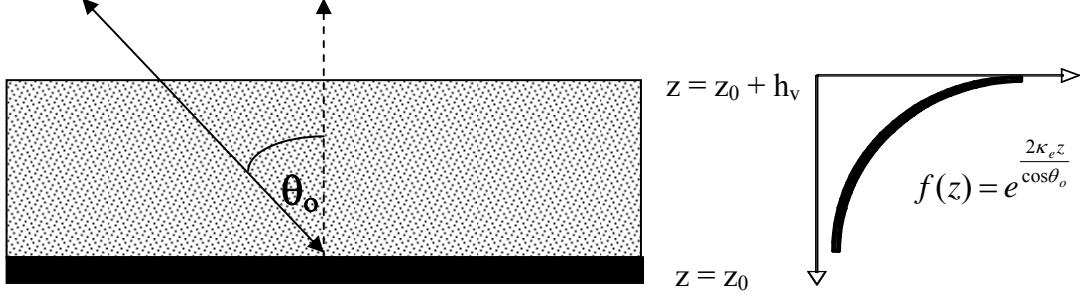


Figure 7: Exponential Structure Function

Rather than expand the exponential function in a Legendre series, it is easier in this case to explicitly evaluate the coherence integrals as shown in equation 26

$$\begin{aligned} \hat{\gamma} &= \mathbf{e}^{ik_z z_0} \frac{m_v \int_0^h e^{\frac{2\kappa_e z}{\cos \theta_0}} e^{ik_z z} dz}{m_v \int_0^h e^{\frac{2\kappa_e z}{\cos \theta_0}} dz} \\ &= \frac{2\kappa_e \mathbf{e}^{ik_z z_0}}{\cos \theta_0 (e^{2\kappa_e h_v / \cos \theta_0} - 1)} \int_0^h e^{ik_z z} e^{\frac{2\kappa_e z}{\cos \theta_0}} dz \\ &= f(h_v, \kappa_e) = \mathbf{e}^{ik_z z_0} \frac{p_1 (e^{p_2 h_v} - 1)}{p_2 (e^{p_1 h_v} - 1)} \quad \left\{ \begin{array}{l} p_1 = \frac{2\kappa_e}{\cos \theta_0} \\ p_2 = \frac{2\kappa_e}{\cos \theta_0} + ik_z \end{array} \right. \quad - 26) \end{aligned}$$

This example illustrates an important point, namely that the coherence in general depends not only on the volume depth h_v but also on the shape of the structure function. The exponential model essentially allows a one-parameter model for variation of structure (via κ_e). High extinction implies an effective scattering layer at the top of the volume. Figure 8 shows an example of how the coherence varies for an exponential profile with varying κ_e and depth h_v . We have selected a baseline corresponding to $k_z = 0.1567$ (which corresponds to a zero of the SINC model at 40m) and considered 45 degrees angle of incidence. Note that for zero extinction we obtain, as a special case, the SINC model again.

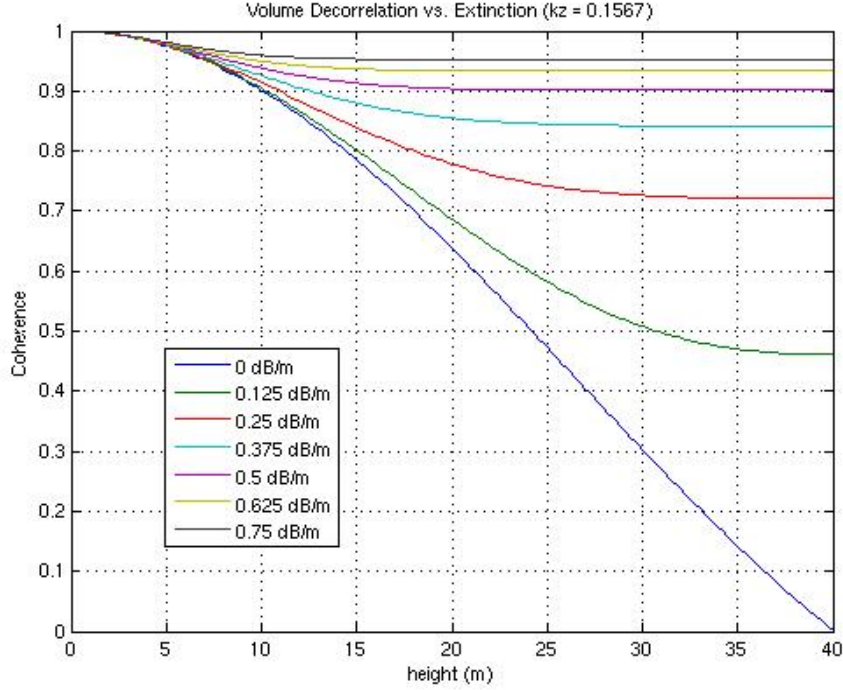


Figure 8 : Volume Decorrelation versus Height for Various Extinctions

However, as extinction increases so the coherence increases for a given height. This arises physically as the effective scattering volume is being squeezed into a smaller and smaller region close to the top of the volume as extinction is increased. This can be confirmed by plotting the phase of the coherence. We first define the fractional phase centre height P_c from the interferometric phase ϕ as shown in equation 27

$$P_c = \frac{\phi}{h_v k_z} \quad - 27)$$

Figure 9 shows how P_c varies with extinction and height. Note that for the special case of zero extinction we obtain a phase centre half way up the layer as expected in the SINC model. However, as the extinction increases we see that the phase centre moves towards the top of the layer, approaching $P_c = 1$ in the limit of infinite extinction.

We have seen from figures 8 and 9 that coherence amplitude and phase variations are linked. Indeed it is instructive to visualise both at the same time by employing the coherence diagram representation. Figure 10 shows how the complex coherence varies inside the unit circle in the complex coherence plane for three extinction values and layer depths varying from 0 to 40m (using the same parameters used in figures 8 and 9). Here we see that the SINC model spirals quickly to the origin i.e. to zero coherence while the high extinction cases show gentler spirals with more rapid phase variation around the unit circle.

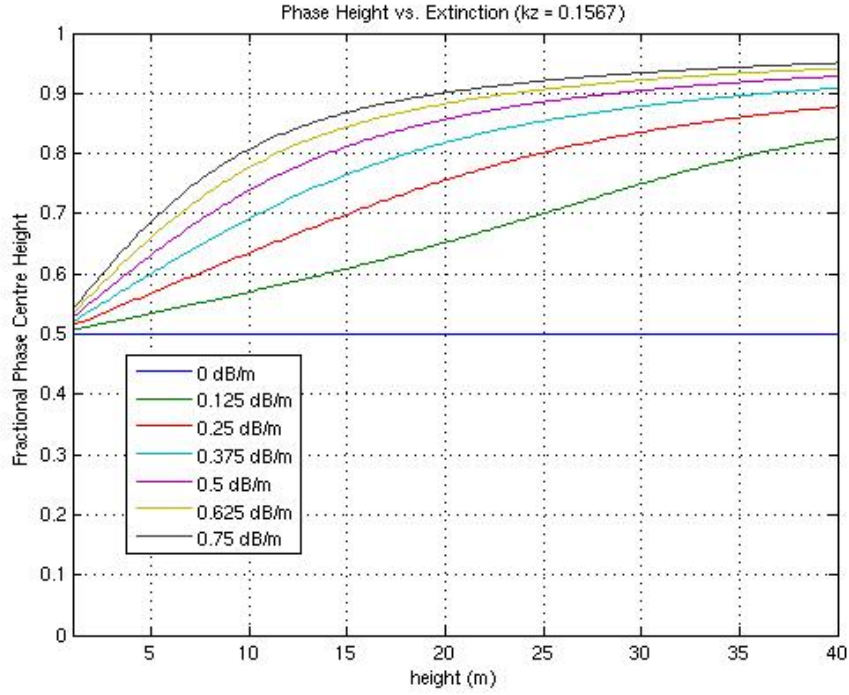


Figure 9 : Phase centre height versus height for various extinctions

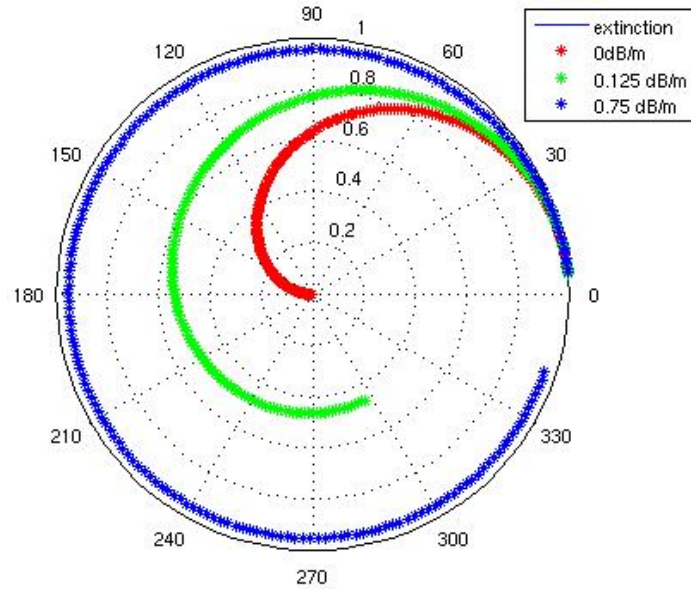


Figure 10: Representation of complex volume coherence variation inside unit circle for varying extinction

Finally we note that extinction can itself be a function of polarization and more generally the scattering within a volume may change with polarization. Hence the interferometric coherence, in contrast to the simple SINC model, may itself depend on polarization. This leads us to consider the application of polarimetric interferometry to general structure function estimation.

1.2.6 Generalised Structure Functions

Finally we consider the most general case, when the structure function can have arbitrary form, as shown schematically in figure 11

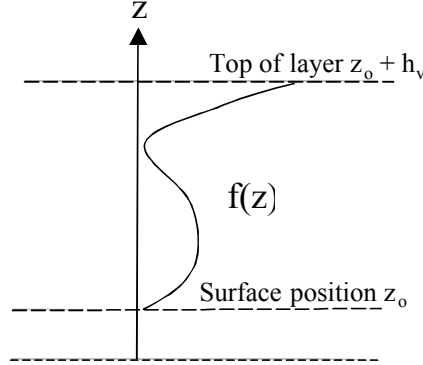


Figure 11: Schematic Representation of a General Structure Function $f(z)$

In this case we make no assumptions about the variation of scattering in the vertical direction other than, without loss of generality, it has unit integral so that

$$\int_0^{h_v} f(z) dz = 1 \quad - 28)$$

This will then allow us to generate a 3-D image by multiplying the profile for a given pixel by the total RCS in the SAR image. We must then consider a general Legendre expansion of the function and relate this to coherence by an infinite series as shown in equation 29

$$\tilde{\gamma} e^{-ik_v} e^{-i\phi_0} = \tilde{\gamma}_k = f_0 + a_{10}f_1 + a_{20}f_2 + ..a_{n0}f_n. \quad - 29)$$

We note that as the order increases, so resolution increases and we can think of the series like a Fourier expansion, with the low ‘frequency’ terms generating the coarse features of the profile and higher frequencies the finer detail. We shall see that with a single baseline interferometer we can only reconstruct a low frequency ‘bandlimited’ form of $f(z)$. Nonetheless this will give us some sensitivity to differences in structure function that can be used for improved parameter estimation and classification products.

Also, we see from figure 6 that the coherence functions get smaller with increasing order of polynomial and this gives some support to the idea that truncating the series at some finite order will lead to only a small error residual. Finally, it is important to realise that these functions apply to arbitrary structures and the differences are then compactly represented by the Legendre spectrum, the set of coefficients a_{10} etc. If we can therefore estimate this set of unknown coefficients by inverting the coherence relation, then we can use them to generate an estimate of the unknown vertical structure profile. We now turn to consider such an approach based on coherence tomography.

1.3 Polarization Coherence Tomography (PCT)

1.3.1 First Order Coherence Model

In order to use the infinite series of equation 29 with real data we must first truncate the series at some finite order. The simplest nontrivial case is to truncate at first order as shown in equation 30. Here we assume that the remainder R_{FL} in equation 30, which is the sum of higher order coherence functions, is always small

$$\tilde{\gamma} = e^{ik_v} e^{i\phi_o} (f_0 + a_{10} f_1 + R_{FL}) \approx e^{i(k_v + \phi_o)} \left(\frac{\sin k_v}{k_v} + i a_{10} \left(\frac{\sin k_v}{k_v^2} - \frac{\cos k_v}{k_v} \right) \right) \quad - 30)$$

With this approximation in place we then have a model with two observations (the amplitude and phase of $\tilde{\gamma}$) and three unknowns, ϕ_0 , $k_v = k_z h_v / 2$, which is a function of the unknown height h_v and known baseline k_z , and a_{10} , a normalised linear Legendre coefficient. Hence we have more unknowns than observations and so in order to be able to invert the model we require additional measurements. Varying the polarization, while keeping the wavelength, sensor geometry and baseline constant, provides a convenient way to add measurement diversity without adding new parameters. Indeed it is reasonable then to assume that k_v , ϕ_0 , f_0 and f_1 all remain invariant to changes in polarization and only the Legendre coefficient a_{10} can change, reflecting changes in the structure function with polarization. The most general polarization combinations arise for a 3–element complex vector called a scattering mechanism \underline{w} as defined in equation 31 [12,16]. This set of complex weights is then used with Quadpool scattering matrix data to form two scalar channels s_1 and s_2 at either ends of the baseline and these are used for radar interferometry.

$$\underline{w} = \begin{bmatrix} w_1 \\ w_2 \\ w_3 \end{bmatrix} = \begin{bmatrix} \cos \alpha \\ \sin \alpha \cos \beta e^{i\xi} \\ \sin \alpha \sin \beta e^{i\psi} \end{bmatrix} \quad -31)$$

$$\Rightarrow \begin{cases} s_1 = w_a (S_{HH}^1 + S_{VV}^1) + w_b (S_{HH}^1 - S_{VV}^1) + w_c (S_{HV}^1 + S_{VH}^1) \\ s_2 = w_a (S_{HH}^2 + S_{VV}^2) + w_b (S_{HH}^2 - S_{VV}^2) + w_c (S_{HV}^2 + S_{VH}^2) \end{cases}$$

In the most general case we can consider adding many polarization channels to the model of equation 30, but in the simplest case we require just two, with scattering mechanisms \underline{w}_1 and \underline{w}_2 , providing then four observations and four unknowns as shown in the pair of equations in equation 32.

$$\begin{aligned} \tilde{\gamma}(\underline{w}_1) &= e^{i(k_v + \phi_o)} (f_0 + a_{10}(\underline{w}_1) f_1) = e^{i\phi} (f_0 + a_{10}(\underline{w}_1) f_1) \\ \tilde{\gamma}(\underline{w}_2) &= e^{i(k_v + \phi_o)} (f_0 + a_{10}(\underline{w}_2) f_1) = e^{i\phi} (f_0 + a_{10}(\underline{w}_2) f_1) \end{aligned} \quad - 32)$$

This is a more balanced set suitable for inversion i.e. for estimation of the four unknown parameters ϕ_0 , k_v , $a_{10}(\underline{w}_1)$ and $a_{10}(\underline{w}_2)$ from two observations of complex coherence. The following strategy follows immediately from equation 32. First we estimate the phase term by differencing the complex coherences as shown in 33

$$\phi = k_v + \phi_o = \arg(-i(\tilde{\gamma}(\underline{w}_1) - \tilde{\gamma}(\underline{w}_2))) \quad - 33)$$

We can then calculate k_v from the real part of the phase shifted coherence as shown in equation 34

$$\text{Re}(\tilde{\gamma}(\underline{w}_1)e^{-i\phi}) = \text{Re}(\tilde{\gamma}(\underline{w}_2)e^{-i\phi}) = \frac{\sin k_v}{k_v} \quad 0 \leq k_v \leq \pi \quad - 34)$$

Note that to conveniently invert this relation to estimate k_v we can use the following approximation for the SINC function, valid over the range 0 to π .

$$\begin{aligned} y = \frac{\sin(x)}{x} &\approx \sin\left(\frac{(\pi-x)}{2}\right)^{1.25} \quad 0 \leq x \leq \pi, \quad 0 \leq y \leq 1 \\ \Rightarrow x &\approx \pi - 2\sin^{-1}(y^{0.8}) \\ \Rightarrow k_v &\approx \pi - 2\sin^{-1}(\text{Re}(\tilde{\gamma}(\underline{w}_2)e^{-i\phi})^{0.8}) \end{aligned} \quad - 35)$$

This, when combined with equation 33, allows us to calculate the surface phase ϕ_0 . Finally we can then calculate the structure parameter for arbitrary polarization \underline{w} from the imaginary part of the phase-shifted coherence as shown in equation 36

$$a_{10}(\underline{w}) = \frac{\text{Im}(\tilde{\gamma}(\underline{w})e^{-i\phi})}{f_1} = \frac{\text{Im}(\tilde{\gamma}e^{-i\phi})k_v^2}{\sin k_v - k_v \cos k_v} \quad - 36)$$

Finally we can then reconstruct the vertical profile by knowing the interferometric wavenumber k_z to calculate the height and then using the Legendre coefficient to reconstruct the profile with unit integral over this height range as shown in equation 37

$$\hat{h}_v = \frac{2k_v}{k_z} \Rightarrow \hat{f}_{L1}(z) = \frac{1}{\hat{h}_v} \left((1 - \hat{a}_{10}) + \frac{2\hat{a}_{10}}{\hat{h}_v} z \right) \quad 0 \leq z \leq \hat{h}_v \quad - 37)$$

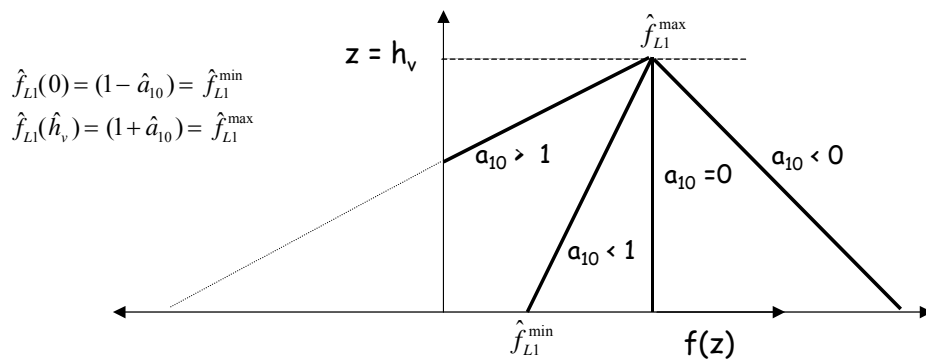


Figure 12 : Summary of first order reconstruction of the vertical structure function

Figure 12 shows a schematic summary of the types of structure function we can construct from this simple first order truncation. We note that the maximum and minimum of this first order structure function are given simply in terms of the parameter a_{10} as shown in equation 38

$$\begin{aligned}\hat{f}_{L1}(0) &= \frac{1}{h_v}(1 - \hat{a}_{10}) = \hat{f}_{L1}^{low} \\ \hat{f}_{L1}(\hat{h}_v) &= \frac{1}{h_v}(1 + \hat{a}_{10}) = \hat{f}_{L1}^{high}\end{aligned}\tag{- 38}$$

Note that for $a_{10} > 1$ this has a negative minimum on the surface. This may seem to violate the important physical requirement that $f(z)$ be non-negative (since physically it represents scattered power as a function of depth). However, such a restriction is not necessary when we realise that $f_L(z)$ is only a band-limited approximation to the true structure function. While the true function is always nonnegative, its approximation can go negative, indicating more concentrated scattering from the top of the layer. To illustrate, we show in figure 13 various Legendre approximations (up to 6th order) for a vertical step function at 50% of layer depth i.e. the true structure function involves scattering only from the top half of the layer. We see that all approximations (including the 1st order as used in $f_L(z)$) go negative at low z values and this is a direct consequence of the true physical structure. Hence it is useful to allow such negative profiles in the estimation, on the understanding that we only ever obtain an approximation to the true profile. If it's important to maintain positivity in the approximation then the negative parts of the profile can be set to zero and the estimate still have some physical correspondence with the true profile.

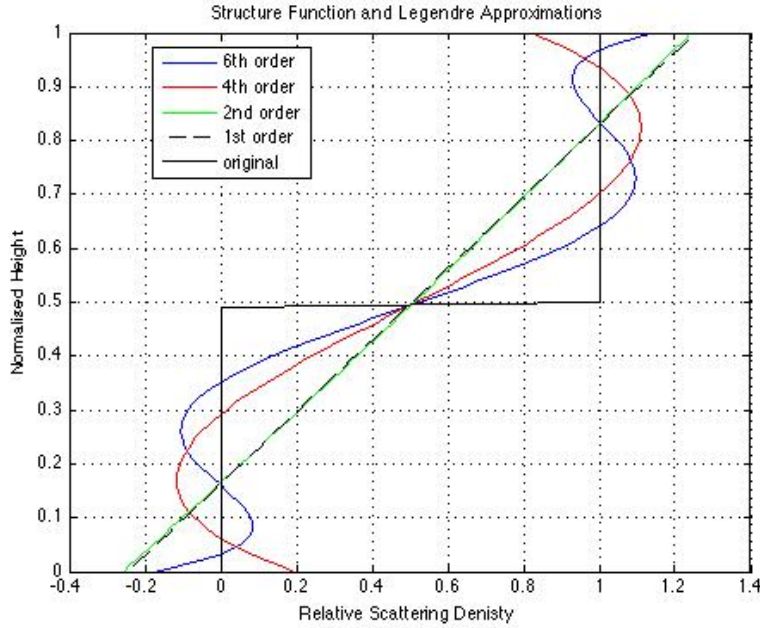


Figure 13: Examples of bipolar structure function estimates of a non-negative true structure function (in black)

Before proceeding further, it is important now to consider the range of the three unknown parameters ϕ_0 , k_v and a_{10} with a view to investigating the uniqueness of this model inversion. The phase ϕ_0 is defined in the range 0 to 2π , with ambiguities arising for surface variations in excess of this. This corresponds to the classical phase unwrapping problem in radar interferometry. However, here we are more concerned with phase shifts relative to ϕ_0 and hence can ignore the phase unwrapping problem, at least initially. If we consider scenarios where k_z is always positive (by appropriate selection of master and slave tracks for the baseline generation so that $\Delta\theta$ is always

positive in equation 8) and h_v is positive then a good working range for k_v is $0 \leq k_v \leq \pi$. Although mathematically k_v can go to infinity, in practice we would wish to restrict it to avoid phase ambiguities in the layer i.e. we design the interferometer to ensure that the depth of the layer is always less than the 2π ambiguity height of the interferometer. This then restricts k_v to the range specified.

The Legendre coefficient a_{10} can be bipolar i.e. negative or positive, but must be constrained so that the magnitude of the right hand side in equation 30 is always less than or equal to one (to match the limits of coherence on the left hand side). This requires the following inequality to hold

$$|\tilde{\gamma}| \leq 1 \Rightarrow |a_{10}| \leq \sqrt{\frac{1-f_0^2}{|f_1|^2}} = \sqrt{\frac{k_v^2 - \sin^2 k_v}{\frac{\sin^2 k_v}{k_v^2} - 2 \frac{\sin k_v \cos k_v}{k_v} + \cos^2 k_v}} \quad - 39)$$

The range of a_{10} allowed under this constraint varies as a function of k_v as shown in figure 14. Note that the range is limited to ± 1.732 for low values of a_{10} up to $\pm\pi$ for large values of k_v .

Note also that the variation of coherence with structure (i.e. k_v fixed and a_{10} variable) is a straight line in the complex plane, intersecting the unit circle at two points corresponding to the limits given in equation 39. It is interesting to look at the variation of this line with k_v . We show such a region in figure 15, where we have removed any topographic phase so that the surface phase is zero and lies at the point O.

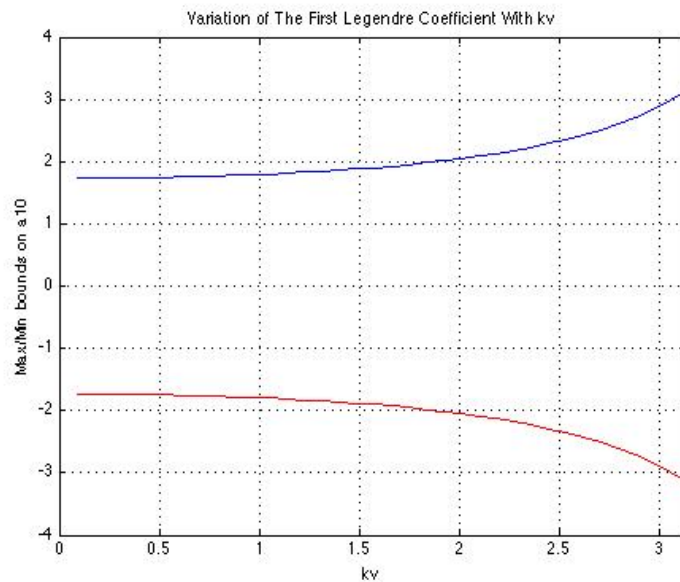


Figure 14: Maximum (blue) and Minimum (red) Bounds on first Legendre Coefficient as a function of k_v

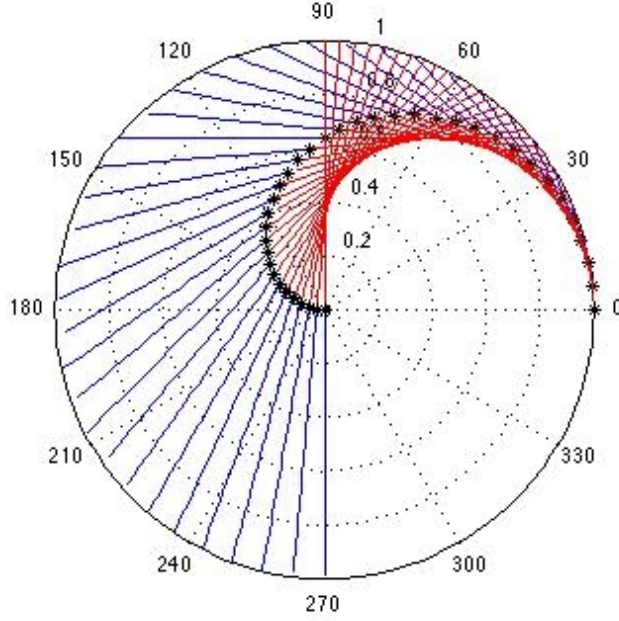


Figure 15 : Coherence Loci for 1st order Legendre Approximation. Positive a_{10} (blue) and negative a_{10} (red) for different k_v values (black stars)

We show a set of lines for variation of k_v from 0 to 180 degrees in 5 degree steps. The loci of points of the uniform SINC model ($a_{10} = 0$) are shown as black stars, which we see constitute a spiral as noted in figure 10. However going through each SINC value is now a straight line (shown in blue for positive a_{10} values and in red for negative). Clearly, if ϕ_0 is not zero then the whole diagram is just rotated clockwise for negative and anticlockwise for positive phase shifts. In any case there are two important observations from this result:

- 1) The first order model does not cover the whole coherence diagram and severely limits the possible set of valid coherences. In fact, for a fixed k_v the valid coherences are constrained to lie along a single straight line going through the appropriate SINC point.
- 2) It follows from this model that the coherence variation with polarization should also lie along a line in the complex plane (see equation 32). However this line does not intersect the unit circle at the topographic phase point, and hence is not the same line as used in other coherence models, such as the 2-layer random-volume-over-ground or RVOG model, widely used and validated in POLInSAR.

We conclude from these observations that the conditions for the inversion scheme of equations 33-37 to apply are very restrictive. Consequently we can consider the first order Legendre model to be inappropriate for general physical applications. At the very least, for fixed k_v , we require better coverage of the complex plane so we can model a wider range of physical scenarios (including the RVOG model). To do this we must extend the model to second order as we now consider.

1.3.2 Second Order Legendre Model

We now consider truncation of the Legendre series to second order, as shown in equation 40. Again we assume we can isolate all polarization dependence in the Legendre spectrum, which amounts to the assumption that height, topographic phase and baseline are all invariant to polarization changes.

$$\tilde{\gamma}(\underline{w}) \approx e^{i(k_v + \phi_o)} \left\{ \frac{\sin k_v}{k_v} + a_{10}(\underline{w}) i \left(\frac{\sin k_v}{k_v^2} - \frac{\cos k_v}{k_v} \right) + a_{20}(\underline{w}) \left(\frac{3 \cos k_v}{k_v^2} - \left(\frac{6 - 3k_v^2}{2k_v^3} + \frac{1}{2k_v} \right) \sin k_v \right) \right\} \quad - 40)$$

We see that now we have two polarization dependent coefficients, a_{10} and a_{20} , which together with k_v and ϕ_0 constitute a set of four unknowns to be determined from the two observations (amplitude and phase of coherence). Here polarization diversity does not seem to help us, each additional \underline{w} adds two observations but also adds two new unknowns. Instead we need to develop a different strategy to invert equation 40. First however we investigate the expanded coverage in the complex plane of this higher order model.

To visualise coverage of the second order Legendre coherence model (equation 40) inside the unit circle, we first rewrite the coherence in the following form

$$\begin{aligned} \tilde{\gamma}(\underline{w}) &= e^{i(k_v + \phi_o)} (f_0 + a_{10}(\underline{w}) f_1 + a_{20}(\underline{w}) f_2) \\ &= z(a_{20}) + a_{10} d \\ \Rightarrow d &= e^{ik_v + \phi} i \left(\frac{\sin k_v}{k_v^2} - \frac{\cos k_v}{k_v} \right) \\ z(a_{20}) &= e^{ik_v + \phi} \left(\frac{\sin k_v}{k_v} + a_{20} \left\{ \frac{3 \cos k_v}{k_v^2} - \left(\frac{6 - 3k_v^2}{2k_v^3} + \frac{1}{2k_v} \right) \sin k_v \right\} \right) \end{aligned} \quad - 41)$$

In this form we see that a_{10} again generates a line in the complex plane going through a fixed-point z with direction d , but now the fixed point is itself determined by the second order coefficient a_{20} . Since the function f_2 is always negative (see figure 6), it follows from equation 41 that for negative a_{20} the fixed point moves radially outwards towards the unit circle and for positive a_{20} it moves inwards towards the origin of the coherence diagram. Hence for a fixed k_v we end up with a family of straight lines, all with the same slope and defined by a set of fixed points generated by a radial line going through the SINC point, as shown in figure 16. Here we show in black the spiralling SINC locus for $\phi_0 = 0$. For each point on this curve there is now a family of lines generated for positive and negative a_{10} (shown as red and blue lines respectively) and moving up and down the radial line through the SINC point according to positive or negative a_{20} . As we move along the SINC locus then this pattern of lines is rotated and shifted accordingly. The bounds of a_{10} for fixed a_{20} can be derived by setting the coherence to unity, as shown in equation 42.

$$\begin{aligned}
|\tilde{\gamma}|^2 &= (f_0 + ia_{10}f_1 + a_{20}f_2)(f_0 - ia_{10}f_1 + a_{20}f_2) \\
&= f_0^2 + 2a_{20}f_0f_2 + a_{10}^2f_1^2 + a_{20}^2f_2^2 = 1 \\
\Rightarrow -\sqrt{\frac{1-(f_0+a_{20}f_2)^2}{f_1^2}} &\leq a_{10} \leq \sqrt{\frac{1-(f_0+a_{20}f_2)^2}{f_1^2}}
\end{aligned} \tag{42}$$

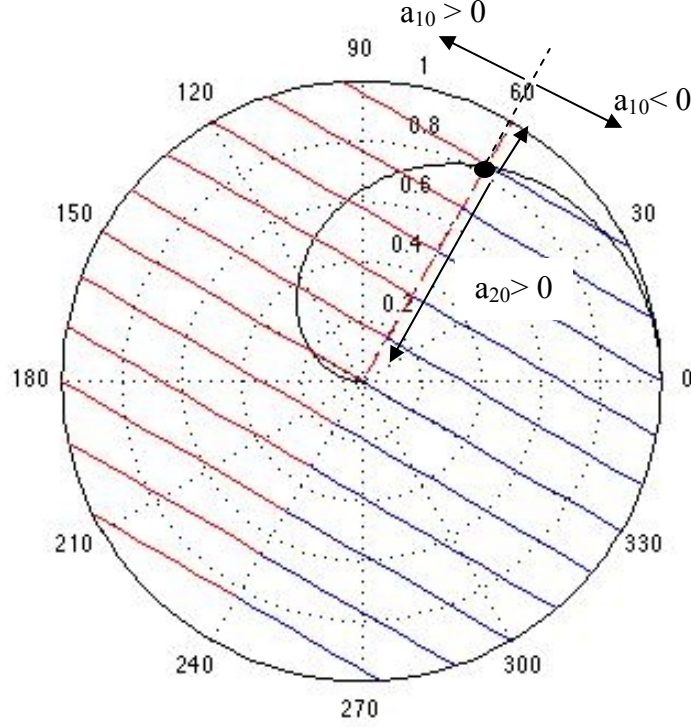


Figure 16: Coherence Loci for the Second Order Legendre approximation

and if we set $a_{10} = 0$ we obtain the corresponding bounds of a_{20} as follows

$$(f_0 + a_{20}f_2)^2 = 1 \Rightarrow \frac{1-f_0}{f_2} \leq a_{20} \leq -\frac{(1+f_0)}{f_2} \tag{43}$$

We note that, for a fixed k_v value, these bounds now lead to full coverage of the unit circle. Hence if we know the k_v value then we can use the position of *any* sample coherence to estimate the two parameters a_{10} and a_{20} as shown in equation 44

$$a_{10}(\underline{w}) = \frac{\text{Im}(\tilde{\gamma}(\underline{w})e^{-i\phi})}{f_1} \quad a_{20}(\underline{w}) = \frac{\text{Re}(\tilde{\gamma}(\underline{w})e^{-i\phi}) - f_0}{f_2} \tag{44}$$

The structure function itself can then be expressed as shown in equation 45

$$\hat{f}_{L2}(\underline{w}, z) = \frac{1}{h_v}(1 - \hat{a}_{10} + \hat{a}_{20}(\underline{w})) + \frac{2z}{h_v}(\hat{a}_{10}(\underline{w}) - 3\hat{a}_{20}(\underline{w})) + \hat{a}_{20}(\underline{w})\frac{6z^2}{h_v^2} \quad 0 \leq z \leq h_v \tag{45}$$

One interesting property of the 2nd order Legendre approximation $\hat{f}_{2L}(z)$ is that its extreme value (maximum or minimum) no longer has to fall at the boundaries of the

layer. This gives us more flexibility in representing variations in the structure function itself. The stationary point of the estimated profile can be simply related to the Legendre coefficients as shown in equation 46

$$\frac{df_{L2}(z)}{dz} = 0 \Rightarrow z_m = h_v \left(\frac{1}{2} - \frac{a_{10}}{6a_{20}} \right) \quad - 46)$$

Here we see for example if $a_{10} = 0$ then the maximum (minimum) of the profile occurs at half the layer depth for positive (negative) a_{20} . In general if the ratio a_{10}/a_{20} is positive then the extreme point will occur in the lower half of the layer while for a negative ratio the extreme point will occur in the upper half. In this way we can represent a much wider variety of structure functions than is possible using the classical RVOG model (which assumes the maximum always occurs at the top of the volume). In particular we note that since a_{20} can be positive or negative we can now represent functions with a maximum response below the top of the layer (negative a_{20}) or with an enhanced response from the surface position at $z = 0$ (a_{20} positive). The former is useful for representing non-exponential volume scattering profiles, while the latter can be used to represent changes in μ the effective surface to volume scattering ratio [13,14].

To see an example of the flexibility of this second order approximation, we consider its application to the 2-layer RVOG model. This model is summarised in equation 47 [13,14]

$$\tilde{\gamma}(\underline{w}) = e^{i\phi_0} \frac{\tilde{\gamma}_v + \mu(\underline{w})}{1 + \mu(\underline{w})} \quad \tilde{\gamma}_v = e^{ik_v} \frac{\sin k_v}{k_v} \quad - 47)$$

For simplicity we show a case where the volume only coherence ($\mu = 0$) is given by a simple zero extinction medium (a uniform structure function). The factor μ then corresponds physically to the ratio of surface-to-volume scattering. We also assume that the surface phase $\phi_0 = 0$ in this example. Figure 17 shows how this model maps onto the Legendre co-ordinates (defined by k_v) for μ in the range -30dB to $+30\text{dB}$ in 1dB steps. Here we have used a specific example when $h_v = 10\text{m}$, $k_z = 0.2$ and so $k_v = 1$. Each point of the RVOG model now has a set of Legendre co-ordinates a_{10}, a_{20} as shown in figure 18. We see that when μ is small the co-ordinates are both zero, corresponding to the assumption of a uniform structure. However as μ increases we see that a_{10} increases in a negative direction while a_{20} increases in the positive direction. This reflects changes in the structure function itself.

Figure 19 shows how the second order approximation to the RVOG structure function varies with μ . Each vertical profile extends over 10m and is normalised so that its integral is unity (as in equation 45). On the left we see the uniform volume scattering profile obtained when $\mu = 0$. As μ increases we see a shift in the structure function to more localised surface scattering, as physically expected in the RVOG model. Again we note that as the surface contribution increases, the second order approximation is forced to go negative at some points in the volume. This again reflects the approximate nature of the truncation rather than any physical interpretation of negative scattering amplitudes.

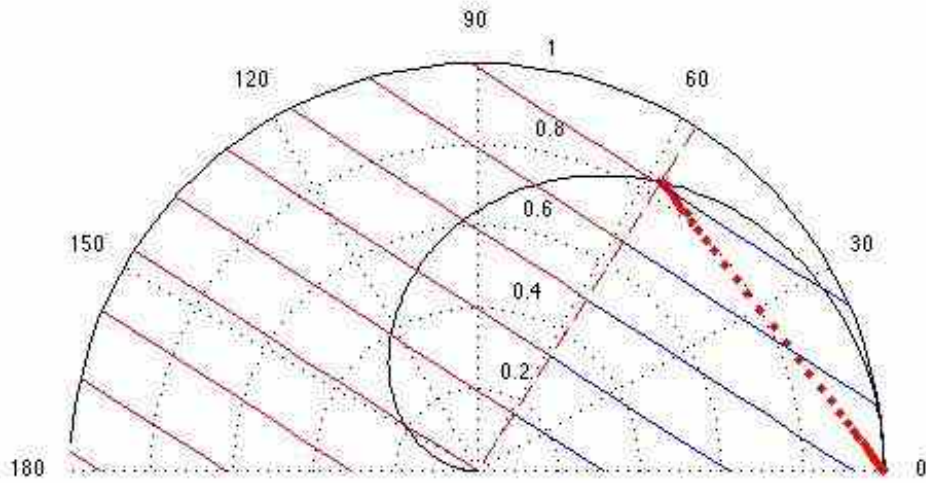


Figure 17: the RVOG Model (in red) superimposed on the 2nd order Legendre Co-ordinate system

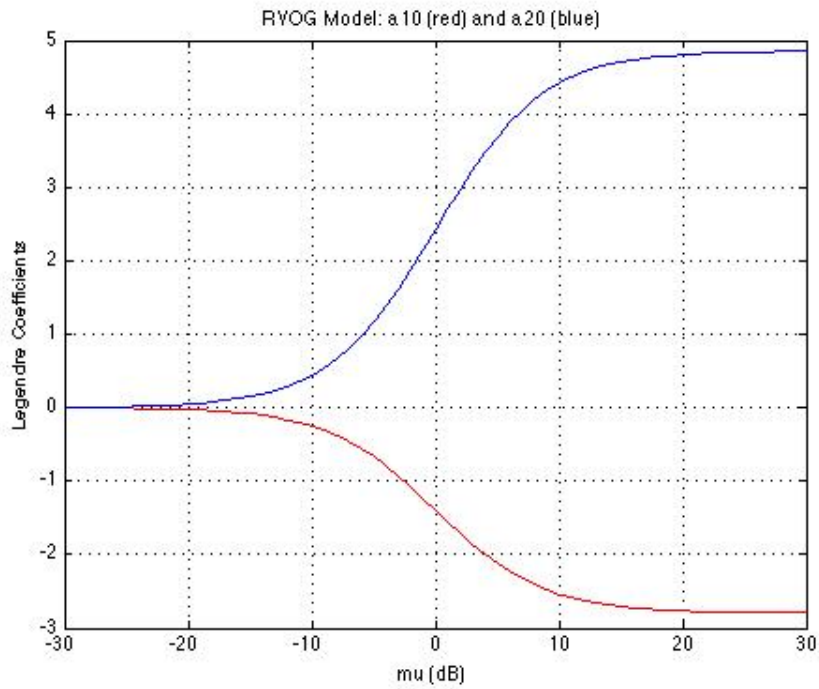


Figure 18: Variation of Legendre Coefficients a_{10} (red) and a_{20} (blue) with μ for the RVOG model

In conclusion we have seen that a second order Legendre expansion is the lowest order truncation capable of providing full unit circle coverage. We have demonstrated its application to the widely used RVOG coherence model to demonstrate its ability to reflect true changes in the underlying structure function. There remains however one issue with this model. It has too many unknowns to be inverted and hence to be applied for tomographic applications. In the next section we turn to consider methods for resolving this limitation.

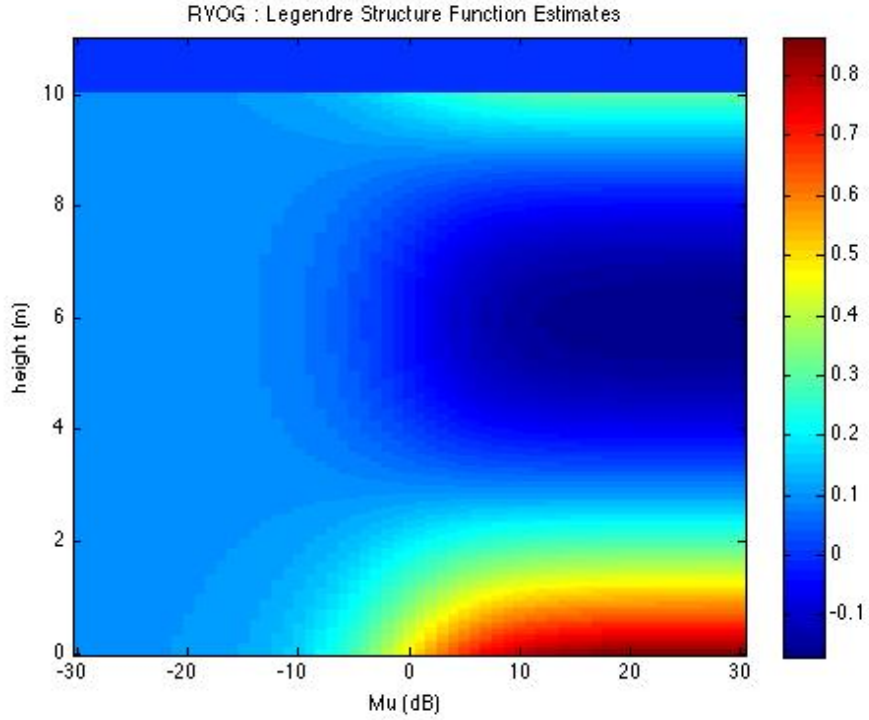


Figure 19: Variation of 2nd order Legendre Structure Function approximation of the RVOG model with surface-to-volume scattering ratio μ

1.4 Parameter Estimation for PCT

In the previous section we showed that a second order truncation of the Legendre series is useful for characterising a wide range of different structure functions. However, for tomographic reconstruction we need to be able to estimate these two parameters from data i.e. to invert the model. The problem with this is that we have more unknowns in the model than observations. For a single polarization channel, single wavelength and single baseline we have only two observations (one complex coherence) while the model has four unknowns (the two Legendre coefficients and two structural parameters ϕ_0 and k_v). The only observation in our favour is that ϕ_0 and k_v are invariant to changes in polarization. Hence in order to do tomography we need somehow to estimate two of these parameters so as to obtain a balance of two unknowns and two observations. In this section we consider approximate methods for doing this. In particular we look at ways of estimating ϕ_0 and k_v so that we can then use these in arbitrary polarization channels to estimate the Legendre spectrum and hence map changes in structure function with polarization. To do this we will see we need to impose some further constraints on properties of the unknown structure function but we will see that these can still be rather lax, allowing still some flexibility (and critically more than in the fixed structure approaches like RVOG) in determining variations in structure.

1.4.1 Surface Phase ϕ_0 Estimation

One of the simplest ideas is to employ a topographic phase estimate based directly on the phase of an interferogram for some suitably selected polarization \underline{w}_s that we know a priori has a structure function close to the bottom of the layer (in the ideal case a Dirac delta function localised at the bottom of the layer). In this way the phase ϕ_0 could then be estimated directly from the phase of the particular interferometric coherence in this channel as shown in equation 48

$$\hat{\phi} = \arg(\tilde{\gamma}_{\underline{w}_s}) \quad 0 \leq \hat{\phi} < 2\pi \quad - 48)$$

This phase could then be used in all other polarizations to reconstruct their particular structure functions. However, we face the problem with this approach of which polarization vector \underline{w} to choose? One immediate physical limitation arises due to the inherently random nature of vector volume scattering, which acts to depolarize the scattered wave with a correspondingly high scattering entropy. This implies that the volume scattering ‘contaminates’ every polarization vector \underline{w} and consequently that it is impossible to find a candidate \underline{w}_s that has a localized structure function. This means that some phase bias will inevitably be present across the whole of polarization space and an approach based on equation 48 will always overestimate the phase. To proceed further we need to consider methods for the systematic removal of this bias. To do this we need first to make some further assumptions about the variation of structure function with polarization.

1.4.1.1 Phase Bias Removal

We can make use of the depolarization caused by volume scattering to help remove the phase bias and improve the accuracy of surface topography estimation as follows. If we make the assumption that the volume scattering component is *completely* random (with azimuthal symmetry and a diagonal polarimetric coherency matrix), then its interferometric coherence contribution will always be invariant to changes in polarization and any combination of surface and volume scattering will then lead to a line in the complex plane. This is just the same assumption made in the RVOG model. The main difference here is that we can now relax the exponential structure assumption used in RVOG and allow the unknown volume coherence term $\tilde{\gamma}_v$ in equation 47 to have arbitrary (but polarization independent) structure function. Clearly by doing this we are restricting the set of valid structure functions. On the other hand the random volume approximation is supported in many applications of POLInSAR (especially forestry) where the inherent complexity of the scattering volume leads to such behaviour.

Importantly, it immediately follows from this assumption that the coherence line intersects the unit circle at the desired surface topography point $e^{i\phi_0}$. Hence if we start by selecting an arbitrary polarization \underline{w}_1 and evaluate its interferometric coherence $\tilde{\gamma}_1$ it will lie somewhere on this line, generally displaced from the desired unit circle point by some unknown phase bias. However, if we now choose a second polarization state \underline{w}_2 , and the only condition we set on \underline{w}_2 is that it have a higher surface-to-volume scattering ratio than the first, so that $\mu_2 > \mu_1$, then it follows that we can find the unit circle point exactly as in POLInSAR inversion as follows.

The idea is to use $\tilde{\gamma}_1$ as a fixed point on the line and relate $\tilde{\gamma}_2$ by a scale factor F_2 along the line towards the unit circle. In this way the two coherences can be related as shown in equation 49. We see that the desired ground topography point is embedded in these equations and we can solve for it directly as shown.

$$\left. \begin{matrix} \tilde{\gamma}_1 \\ \tilde{\gamma}_2 = \tilde{\gamma}_1 + F_2(e^{i\phi} - \tilde{\gamma}) \end{matrix} \right\} \Rightarrow e^{i\phi} = \frac{\tilde{\gamma}_2 - \tilde{\gamma}_1(1 - F_2)}{F_2} \quad 0 \leq F_2 \leq 1 \quad - 49)$$

Here we see that the phase term is obtained as a weighted average of the two complex coherences. If F_2 tends to unity then it represents the desired surface point and $\tilde{\gamma}_2$ is taken as the solution. However in general, as discussed above, there will be phase bias present in both channels and hence this mixture formula is required to compensate for this bias. There remains a problem in that to solve for the surface topography we first require an estimate of the factor F_2 . This can be obtained from the estimated coherences $\hat{\gamma}_1$ and $\hat{\gamma}_2$ directly by forming the product $e^{i\phi}e^{-i\phi} = 1$ using equation 49 to obtain a quadratic. Taking the root that makes F_2 positive, we obtain the solution shown in equation 50

$$\begin{aligned} \hat{\phi} &= \arg(\hat{\gamma}_2 - \hat{\gamma}_1(1 - F_2)) \quad 0 \leq F_2 \leq 1 \\ AF_2^2 + BF_2 + C &= 0 \Rightarrow F_2 = \frac{-B - \sqrt{B^2 - 4AC}}{2A} \quad - 50) \\ A &= |\tilde{\gamma}_1|^2 - 1 \quad B = 2\text{Re}((\tilde{\gamma}_2 - \tilde{\gamma}_1)\tilde{\gamma}_1^*) \quad C = |\tilde{\gamma}_2 - \tilde{\gamma}_1|^2 \end{aligned}$$

Note that, unlike the simple phase algorithm (equation 48), this requires coherence estimates in both amplitude and phase and hence is susceptible to non-compensated errors in coherence such as those due to SNR or temporal effects. Also of course the estimates of coherence themselves have some variance due to their stochastic nature and the effective number of looks (ENL) used in the estimator. Hence for stability of the phase estimate we need to make sure that F_2 is as large as possible (if F_2 tends to zero so that the two points are close together then large errors can result). Hence some care is required in the selection of \underline{w}_1 and \underline{w}_2 . There are two strategies used in making an appropriate selection:

1.4.1.2 Physics based polarization selection.

In this case we use our understanding of surface and volume scattering mechanisms to select the two channels [16]. For example the low frequency Bragg surface model predicts zero or very low levels of cross polarization HV from a flat surface. On the other hand volume scattering from a cloud of anisotropic particles can yield high levels of HV. Hence HV is often chosen as a candidate for the \underline{w}_1 channel. The \underline{w}_2 channel can likewise be selected on the assumption that specular second order (dihedral or double bounce) scattering is dominant and HH-VV is a good choice, when full Quadpol data (HH, HV, VH and VV) is used, with the single channel HH a good fall back when only dual polarised (HH and HV) data is available. Given the physics of double bounce scattering these are both likely to satisfy the requirement

than $\mu_2 > \mu_1$. However in general both will be suboptimal and better use can be made of the polarimetric data by using coherence optimisation as we show in the next section. In summary the direct physics based choice approach makes allocations of the two channels such as those shown in equation 51. Other fixed possibilities can be made but the principle is established, that is to use physical models to select fixed polarizations for channels 1 and 2.

$$\begin{array}{lll} \text{QUADPOL DATA} & \tilde{\gamma}_1 = \tilde{\gamma}_{HV} & \tilde{\gamma}_2 = \tilde{\gamma}_{HH-VV} \\ \text{DUALPOL DATA} & \tilde{\gamma}_1 = \tilde{\gamma}_{HV} & \tilde{\gamma}_2 = \tilde{\gamma}_{HH} \end{array} \quad - 51)$$

In contrast, we can propose a second approach whereby the polarizations 1 and 2 are adaptively selected according to some cost function. We now turn to consider such techniques based on the idea of coherence optimisation.

1.4.1.3 Phase Optimisation

The optimum pairing of polarization vectors \underline{w}_1 and \underline{w}_2 to choose for a line fit would be those with the largest separation in the complex plane. Such a choice would minimise the impact of any fluctuation errors in the estimation of the coherences themselves. One way to find these is to employ phase optimisation [12,17,18,19,20] as we now demonstrate. In this method we employ fully polarimetric data to calculate the following eigenvalue problem as a function of a ‘free’ parameter ϕ .

$$\begin{aligned} [T]^{-1}[\Omega_H(\phi)]\underline{w} &= \lambda(\phi)\underline{w} & \begin{cases} [\Omega_H] = \frac{1}{2}(\Omega_{12}e^{i\phi} + \Omega_{12}^*e^{-i\phi}) \\ [T] = \frac{1}{2}(T_{11} + T_{22}) \end{cases} \\ \Rightarrow \max_{\phi} |\lambda_{\max}(\phi) - \lambda_{\min}(\phi)| & \quad - 52) \\ \Rightarrow \begin{cases} \lambda_{\max} \rightarrow \underline{w}_{\max} \rightarrow \tilde{\gamma}_{\max} \\ \lambda_{\min} \rightarrow \underline{w}_{\min} \rightarrow \tilde{\gamma}_{\min} \end{cases} \end{aligned}$$

For each phase angle ϕ we then find the distance between the maximum and minimum eigenvalues (which correspond to the real part of the coherence). By finding the maximum of this distance *over all* ϕ , we then automatically find the maximum separation and hence align the solution with the axis of the RVOG linear coherence region. We can then find the polarization scattering mechanisms \underline{w}_{\max} and \underline{w}_{\min} from the corresponding eigenvectors. From these we can then derive the two coherence $\tilde{\gamma}_{\max}$ and $\tilde{\gamma}_{\min}$ for use in the topographic phase estimation algorithm of equation 50.

1.4.1.4 Rank Ordering of Coherence Optima

In the previous section we showed how to obtain two special polarization states \underline{w}_{\max} and \underline{w}_{\min} , which have the property that the separation of their interferometric coherences is maximised in the unit circle. However we have to choose an ordering of the two coherences, remembering that we must ensure $\mu_2 > \mu_1$ to find the correct

topography point using equation 50. In fact this is a general problem with all phase bias removal algorithms based on the assumption of a linear coherence region [14]. By definition, a line intersects the unit circle at two points (see figure 20). One is the true topographic phase and the other represents a false solution obtained for the line fit technique by exchanging the rank order of coherences.

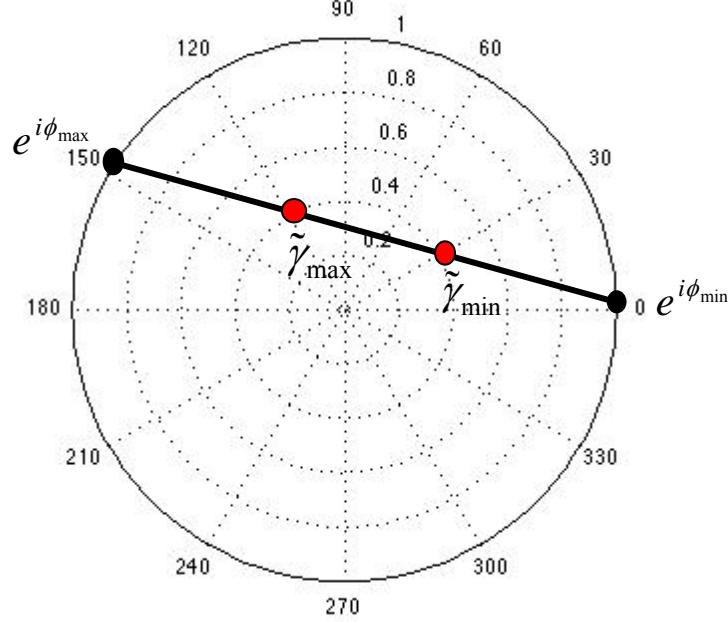


Figure 20 : Unit circle phase ambiguity in POLInSAR

There are several ways to resolve this rank-ordering dichotomy, two common techniques are to use physical arguments based on scattering theory and/or use a comparison of the interferometric phase bias levels of the two solutions.

In the physical approach we again employ our knowledge of the physics of polarimetric scattering to help identify the channel with the highest μ value. The surface dominated channel (highest μ) should for example have a scattering vector close to the form \underline{w}_s shown in equation 53, where α is less than $\pi/4$ for direct surface scattering and greater than $\pi/4$ for specular second order scattering.

$$\left. \begin{array}{l} \underline{w}_s = [\cos \alpha \quad \sin \alpha e^{i\varphi} \quad 0]^T \\ \underline{w}_v = [0 \quad 0 \quad 1]^T \end{array} \right\} \xrightarrow{\mu_s > \mu_v} \begin{cases} \tilde{\gamma}_1 = \tilde{\gamma}_{\min} & \text{if } \left| \underline{w}_{\max}^{*T} \underline{w}_v \right| < \left| \underline{w}_{\min}^{*T} \underline{w}_v \right| \\ \tilde{\gamma}_1 = \tilde{\gamma}_{\max} & \text{if } \left| \underline{w}_{\max}^{*T} \underline{w}_v \right| > \left| \underline{w}_{\min}^{*T} \underline{w}_v \right| \end{cases} \quad - 53)$$

Similarly the orthogonal state \underline{w}_v should match the volume scattering (and have a lower μ). In this way we can develop an algorithm for assigning the optimum phase states in the correct rank order by projecting the eigenvectors onto predetermined ‘reference’ states as shown on the right hand side of equation 53.

In the second approach, we decide on rank ordering by employing the interferometric phase difference between the calculated unit circle intersection point and assumed low μ coherence. Knowing that the volume is above (or below) the surface allows us to calculate these phase differences using the same clockwise (or counter clockwise)

rotation around the coherence diagram (for positive k_z). If we repeat this for both rank permutations then one of the phase shifts will be much larger than the other and can be rejected (especially if it is known that the layer depth is much less than the π height of the interferometer). If we define ϕ_{\max} as the unit circle phase estimate obtained when we propose $\tilde{\gamma}_{\max}$ as the high μ channel estimate and likewise ϕ_{\min} when we propose $\tilde{\gamma}_{\min}$ then we can decide on the most likely rank ordering as shown in 54.

$$\left. \begin{aligned} \Delta_{\max} &= \arg(\tilde{\gamma}_{\min} e^{-i\phi_{\max}}) \\ \Delta_{\min} &= \arg(\tilde{\gamma}_{\max} e^{-i\phi_{\min}}) \end{aligned} \right\} \rightarrow \begin{cases} \tilde{\gamma}_1 = \tilde{\gamma}_{\min} & \text{if } \Delta_{\max} < \Delta_{\min} \\ \tilde{\gamma}_1 = \tilde{\gamma}_{\max} & \text{if } \Delta_{\max} > \Delta_{\min} \end{cases} \quad - 54)$$

So for example in figure 20, if we assume that the volume is above the surface for anticlockwise phase rotation then $\Delta_{\max} = 240^\circ$ and $\Delta_{\min} = 180^\circ$ and hence according to equation 54 we would select $\tilde{\gamma}_1 = \tilde{\gamma}_{\max}$ on the assumption that the layer thickness should be less than the π height of the interferometer.

In practice of course combinations of these two tests can be used, depending on the level of confidence in the scattering mechanisms present in the scene and the knowledge of typical heights in the scene compared to the interferometric baseline.

In conclusion we have seen that we can obtain an estimate of one of the structural parameters, namely ϕ_0 , by fitting a line to the complex coherences for two polarizations. We now turn to consider methods for estimating the remaining parameter, k_v .

1.4.2 Height Estimation Algorithms for PCT

In the previous section we saw that as long as we can assume that the volume scattering contribution to the structure function is random and all polarization dependence comes from a surface contribution, we can employ a straight line fit to estimate surface topography ϕ_0 . There remains now just one other structural parameter to determine, namely k_v . This parameter is found from the product of interferometric wavenumber and height. The former we can always calculate from the system baseline geometry and so the problem reduces to estimation of height h_v . Now we know that polarimetric interferometry has been widely used for height estimation [4,5,14] and so it would be interesting to see if we can employ these techniques in some way. The biggest problem is that in ‘standard’ RVOG height estimation using POLInSAR, assumptions are made about the structure function, namely that it is exponential. However here we wish to preserve information, as far as possible, about different structure functions and so need somehow to develop a structure invariant form of height estimation. In this section we show how this can be obtained, at least in an approximate way.

One of the simplest approaches to estimate height is to use the phase difference between interferograms. In general terms we try to estimate the coherence in two polarization channels, one \underline{w}_v which is volume scattering only and has a phase centre near the top of the layer and a second \underline{w}_s which is surface dominated and has a phase centre near the surface. By forming the phase difference between these interferograms

and scaling by the interferometric wavenumber k_z we then obtain the following estimation algorithm for height and therefore k_v

$$\hat{h}_v = \frac{\arg(\tilde{\gamma}_{w_v} \tilde{\gamma}_{w_s}^*)}{k_z} \Rightarrow k_v = \frac{1}{2} \arg(\tilde{\gamma}_{w_v} \tilde{\gamma}_{w_s}^*) \quad - 55)$$

where again the $\arg(\cdot)$ function is defined in the range 0 to 2π . Although this is a simple algorithm to implement it has some severe drawbacks that mean the height estimate so obtained is generally underestimated. The problems stem from the difficulty in finding polarizations with phase centres exactly at the top and bottom of the layer. To overcome this limitation, the bottom phase component can conveniently be replaced with the topographic phase ϕ_0 , estimated in the previous section. In this way a better estimate of k_v can be obtained as shown in equation 56

$$k_v \approx \frac{1}{2} \arg(\tilde{\gamma}_{w_v} e^{-i\phi_0}) \quad - 56)$$

However, we still face the problem of choosing a volume channel with a phase centre high in the volume. One obvious candidate is to employ one of the phase optimisation states used in ϕ_0 estimation. According to our idea of a random volume above a polarised surface return, the coherence furthest from ϕ_0 will have the highest phase centre in the volume and hence be the best estimate of the volume only scattering channel. However, as noted earlier in figure 9, this phase centre separation can lie anywhere between half-way and the top of the layer and hence in general 56 still underestimates the true height. However, one key idea is that this error can be at least partly compensated by employing a coherence amplitude correction term. The idea is that as the phase centre separation increases so, *at the same time*, the effective volume depth decreases (as the structure function becomes more localised near the top of the layer) and hence the level of volume decorrelation will decrease. A convenient invertible model for this process is just the f_0 or SINC coherence function, as discussed in equation 35. Just as required, when coherence amplitude decreases so this height (or k_v) estimate will decrease at the same time as the phase estimate increases. By combining these two terms we then obtain an approximate algorithm that can compensate some variations in structure as shown in equation 57

$$k_v = \frac{1}{2} \left\{ \arg(\tilde{\gamma}_{w_v} e^{-i\phi_0}) + \varepsilon (\pi - 2 \sin^{-1}(|\tilde{\gamma}_{w_v}|^{0.8})) \right\} \quad - 57)$$

The first term represents the phase component. The second the coherence amplitude correction and ε is a weight, to be selected so as to make the full expression as robust as possible to changes in the structure function. This expression has the right kind of behaviour in two important special cases, if the medium has a uniform structure function then the first term will give half the height or $k_z h_v / 2$ (see figure 9), but the second will then also obtain half the true height and yield $k_z h_v / 2$ (if we set $\varepsilon = 1$) so half the sum gives the correct k_v estimate. At the other extreme, if the structure function in the volume channel is localised near the top of the layer, then the phase height will give the true height $k_z h_v$ and the second term will approach zero. Half the sum then still gives the correct k_v estimate. The idea is that equation 57 will provide a reasonable estimate for arbitrary structure functions between these two extremes. It

requires estimates of only two parameters, the true surface topographic phase ϕ_0 , which follows from equation 50, and the volume only complex coherence. Both of these can be obtained from phase optimisation using Quadpol POLInSAR data.

We can extend this idea further and estimate an optimum value of weighting factor ε by using the second order Legendre structure model for the volume coherence channel as shown in equation 58.

$$\tilde{\gamma}(\underline{w}_v) = e^{i(k_v + \phi_0)} (f_0 + a_{10}(\underline{w}_v)f_1 + a_{20}(\underline{w}_v)f_2) \quad - 58$$

Now if we allow a_{10} and a_{20} their full range then we can fit this coherence to any k_v value and hence seem to undermine the approximation proposed in equation 57. However by making some reasonable physical assumptions about volume scattering we can reduce the range of a_{10} and a_{20} as follows.

The basic idea is that in the selected special volume-only channel there is no surface scattering component and hence the structure function should have a local minimum at the surface ($z = 0$). This requires that, in this polarization channel \underline{w}_v , we restrict $a_{10} \geq 0$ and $a_{20} \leq 0$. When combined with the limits derived in equations 42 and 43 we will see that this constrains the k_z values satisfying equation 58. Figure 21 illustrates the results. Here we show along the abscissa a set of true k_v values in steps of 0.1 over the range 0 to 2.

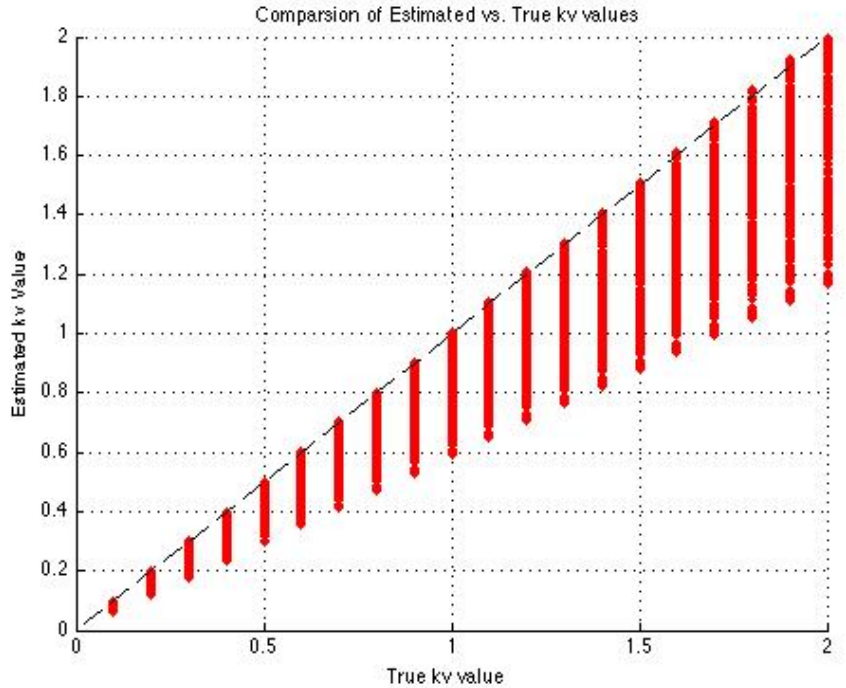


Figure 21: Estimated vs. true k_v values for the full range of volume structure functions a_{10} , a_{20} and using $\varepsilon = 0.8$ in equation 57.

The corresponding ordinate shows the spread of estimated k_v values obtained using equation 57 with $\varepsilon = 0.8$. This value is selected to fit the $a_{20}=0$ variation and the underestimates we see are then entirely due to the presence of nonzero a_{20} structure. It

also ensures that equation 57 will always estimate the minimum height consistent with the data. While the trend in figure 21 is encouraging, some of the errors can apparently be quite large. For example if the estimate yields a value of 1 (in the ordinate of figure 21) then we see that the true value could actually lie anywhere between 1 and 1.6, depending on the volume structure. However this simple interpretation masks an important issue. The underestimation errors for each abscissa point in figure 21 increase in proportion to a_{20} as shown for the $k_v=2$ case in figure 22. Here we plot the fractional error in k_v estimate for all valid values of a_{10} and a_{20} .

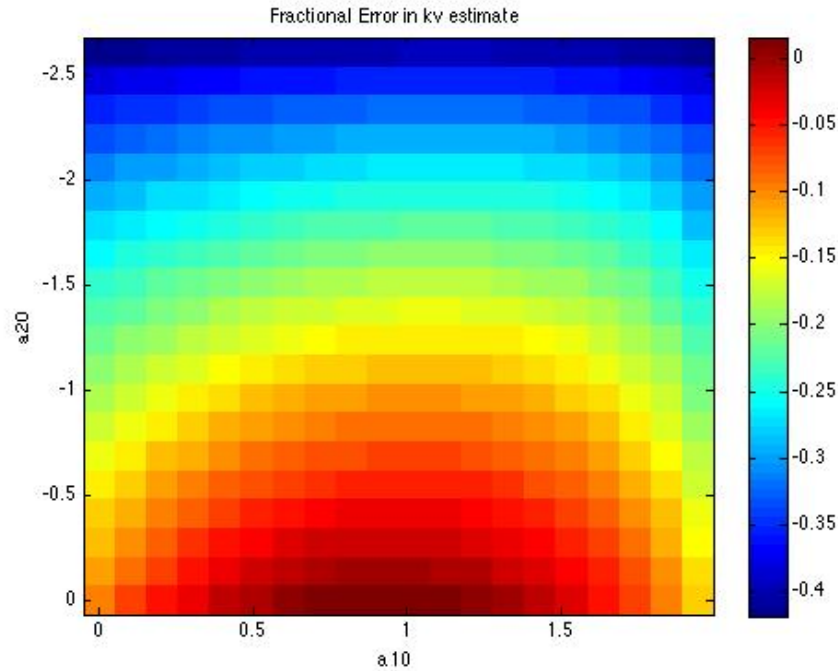


Figure 22: Fractional error for full range of volume structure functions for $k_v = 2$

Note that this behaviour is typical of all other values of k_z and so our conclusions will apply for all values. The key observation from figure 22 is that the largest errors always occur for large a_{20} values. This makes physical sense, as demonstrated in figure 23. Here we show the set of structure functions corresponding to $a_{10} = 0$ and the maximum a_{20} value for all k_v . This is just a quadratic profile, which is a second order approximation to a Dirac delta function located half-way up the volume. In this case we can achieve a combined high coherence and low phase centre, in contradiction to the assumption behind equation 57. This is a problem faced by all radar height estimation techniques based on interferometry. If the volume has a top height h_v but the bulk of the scattering comes from half way up the volume then the radar interferometry ‘sees’ a smaller effective height. In order to resolve such ambiguities we need to add extra information beyond a single baseline single wavelength interferometer. Other possibilities include adding more baselines, a different frequency or others sensor methods such as Lidar (which can measure top height very accurately) or in-situ measurements based on direct height measurements or allometric relationships between height and biomass or diameter at breast height dbh.

If we accept that such errors can occur for a single baseline, but only for rather extreme cases of the structure function, then we can proceed to employ equation 57 as

a reasonable approximation with around 10-15% errors for a wide range of structure function variations.

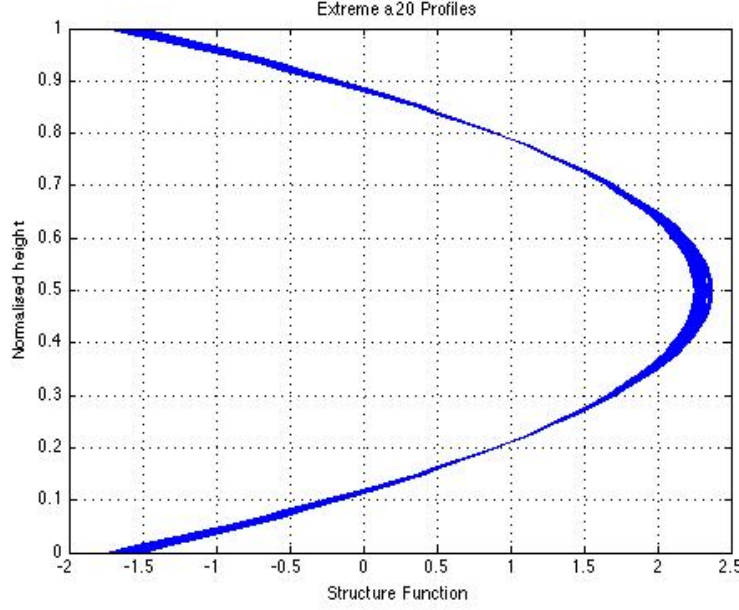


Figure 23: Normalised Structure functions for $a_{10}=0$ and the minimum a_{20} value in volume scattering for all k_v values in range 0 to 2

Before proceeding to our final form of the PCT algorithm, we first show how system error effects can be included in this formalism. The above analysis is based on volume decorrelation only and ignores two important system distortion effects, namely loss of coherence due to signal-to-noise ratio and temporal decorrelation, which is a major factor in repeat pass systems. These can be included in the general scheme and their influence on estimation of the Legendre spectrum investigated as follows.

1.4.3 Inclusion of temporal and SNR decorrelation effects in PCT

The effect of poor signal-to-noise ratio is to provide a polarization sensitive radial shift of the coherence towards the origin of the coherence diagram as follows. The level of SNR decorrelation is given in terms of the signal to noise ratio SNR as shown in equation 59

$$\gamma_{snr}(\underline{w}) = \frac{SNR(\underline{w})}{1 + SNR(\underline{w})} \quad - 59)$$

So for example, if the SNR is 10dB or more, the SNR decorrelation will be 0.9 or above. This factor multiplies any other contributions to coherence. Whether this is a major problem or not therefore depends on the relative contributions of volume and SNR effects, as shown in equations 61 and 62. This error source is likely to be more of a problem in polarization channels with low backscatter, such as the crosspolarised HV channel over bare surfaces, but for most situations where random volume scattering is involved (which depolarizes and hence provides backscatter across all polarizations), there will be little variation with polarization.

On the other hand, temporal decorrelation can be much more important, especially in the presence of temporally unstable scatterers, as occurs in scattering by wind blown vegetation. To further complicate issues, the effects of temporal changes may not be uniform across the structure function. For example wind blown motion may affect the top of the vegetation layer more than the lower regions. To accommodate this we can modify the basic coherence integrals in equation 13 to include in the numerator (I_2) a new temporal structure function $g(z)$ as shown in equation 60

$$\left. \begin{aligned} I_2 &= e^{ik_z z_0} \int_0^h g(z') f(z') e^{ik_z z'} dz' \\ I_1 &= \int_0^h f(z') dz' \end{aligned} \right\} \Rightarrow \tilde{\gamma} = \frac{I_2}{I_1} \quad - 60)$$

The function $g(z)$ will vary between 0 and 1, being zero in regions of maximum change and 1 for zero change. In terms of a Legendre expansion, $g(z)$ will of course have its own expansion coefficients, which will be different in general to those of $f(z)$ and hence the effect of temporal decorrelation must formally be evaluated as a product of Legendre series in the numerator I_2 . In the simplest case however we can just assume that $g(z) = \gamma_t$, a constant function with height, in which case the total coherence can be expressed as shown in equation 61

$$\tilde{\gamma}(\underline{w}) = \gamma_{SNR} \gamma_t e^{ik_z z_0} e^{i \frac{k_z h_v}{2}} (f_0 + a_{10}(\underline{w}) f_1 + a_{20}(\underline{w}) f_2) \quad - 61)$$

Hence we see that, in the simplest case, signal-to-noise ratio and temporal decorrelation effects can be included in the PCT formalism by including them as scalar multiplying factors of the observed coherence. Hence neither distorts the mean phase of the complex coherence but reduces the coherence amplitude (and hence increases phase variance). To see the effects on PCT, we can rewrite the estimation of the 2nd order Legendre spectrum (for known ϕ_0 and k_v) as a matrix inversion problem as shown in equation 62

$$\begin{aligned} \begin{bmatrix} a_{00} \\ a_{10} \\ a_{20} \end{bmatrix} &= \begin{bmatrix} 1 & 0 & 0 \\ 0 & f_1 & 0 \\ 0 & 0 & f_2 \end{bmatrix}^{-1} \begin{bmatrix} 1 & 0 & 0 \\ 0 & \gamma_{snr} \gamma_t & 0 \\ 0 & 0 & \gamma_{snr} \gamma_t \end{bmatrix}^{-1} \begin{bmatrix} 1 \\ \text{Im}(\tilde{\gamma}_k) \\ \text{Re}(\tilde{\gamma}_k) \end{bmatrix} - \begin{bmatrix} 1 & 0 & 0 \\ 0 & f_1 & 0 \\ 0 & 0 & f_2 \end{bmatrix}^{-1} \begin{bmatrix} 0 \\ 0 \\ f_0 \end{bmatrix} \\ &\Rightarrow \begin{aligned} a_{00} &= 1 \\ a_{10} &= \frac{\text{Im}(\tilde{\gamma}_k)}{f_1 \gamma_{snr} \gamma_t} \\ a_{20} &= \frac{\text{Re}(\tilde{\gamma}_k)}{f_2 \gamma_{snr} \gamma_t} - \frac{f_0}{f_2} \end{aligned} \end{aligned} \quad - 62)$$

As shown, the effect of temporal and SNR effects will be to amplify errors in the Legendre spectrum estimation. From figure 6 we also see that $|f_2| \ll |f_1|$ and so from equation 62 it follows that any errors in coherence will be amplified most in the second order coefficient. The impact of these errors will depend on the magnitude of the product $\gamma_t \gamma_{snr}$ compared to the functions f_1 and f_2 . Since these latter both increase with increasing baseline (see figure 6), noise and SNR effects will be most prominent

for small baselines, and their relative impact will decline with increasing baseline. This gives us one way to combat such effects, by working at larger baselines in repeat pass scenarios for example. A second key way to combat temporal effects is to operate at longer wavelengths, as these give less temporal decorrelation for a given motion of the scatterers. Hence the combination of long wavelength, large baseline polarimetric interferometry is well suited to PCT applications. However it is clear that the best overall performance is obtained by avoiding temporal effects altogether by employing a single pass sensor. Such a sensor (as long as it has high enough SNR) can be operated with a smaller baseline than repeat pass, because there is then less need to counteract the effects of $\gamma_t \gamma_{\text{snr}}$ in equation 62.

However, there are some further complications associated with $\gamma_t \gamma_{\text{snr}}$ when we wish to use the data to not only estimate the Legendre spectrum, but also estimate topographic phase ϕ_0 and height h_v . The good news is that as long as temporal effects are restricted to the volume component (which is assumed random) and SNR is high enough, then the straight-line approach of equation 50 is still maintained, albeit with increased phase noise due to the lower coherence. So the same algorithm can still be applied to estimate surface phase. The effect on height and k_v estimation is however more subtle, as shown in equation 63. Loss of coherence due to temporal or SNR effects will not change the mean phase difference in the first term but will reduce the effective coherence in the second. This will act to overestimate the coherence component of the sum and hence overestimate k_v .

$$k_v = \frac{1}{2} \left\{ \arg(\gamma_{\text{snr}} \gamma_t \tilde{\gamma}_{w_v} e^{-i\phi_0}) + 0.8(\pi - 2 \sin^{-1}(|\gamma_{\text{snr}} \gamma_t \tilde{\gamma}_{w_v}|^{0.8})) \right\} \quad - 63)$$

1.5 Summary Algorithm for Polarization Coherence Tomography (PCT)

In summary we can propose the following processing steps needed to generate a 3-D image from single baseline, single frequency POLInSAR data using coherence tomography:

Stage 1: Isolate Two Reference Polarization Channels

Isolate candidates for the two volume and surface dominated polarization channels \underline{w}_1 and \underline{w}_2 (using physical models or phase/coherence optimisation) and calculate the corresponding interferometric complex coherences $\tilde{\gamma}_1$ and $\tilde{\gamma}_2$

Stage 2: Phase Bias Removal and ϕ_0 estimation

Use these two coherences in the appropriate order to estimate ϕ_0 from a line fit as shown in equation 64

$$\begin{aligned} \hat{\phi}_0 &= \arg(\tilde{\gamma}_2 - \tilde{\gamma}_1(1 - F_2)) \quad 0 \leq F_2 \leq 1 \\ AF_2^2 + BF_2 + C &= 0 \Rightarrow F_2 = \frac{-B - \sqrt{B^2 - 4AC}}{2A} \\ A &= |\tilde{\gamma}_1|^2 - 1 \quad B = 2\text{Re}((\tilde{\gamma}_2 - \tilde{\gamma}_1) \cdot \tilde{\gamma}_1^*) \quad C = |\tilde{\gamma}_2 - \tilde{\gamma}_1|^2 \end{aligned} \quad - 64)$$

Stage 3 : k_v estimation, with compensation for any temporal decorrelation

Identify a volume polarization channel \underline{w}_v (either from physical modelling or appropriate selection of optimum states \underline{w}_1 and \underline{w}_2) and calculate k_v (with some correction for γ_t and γ_{snr} if known) as shown in 65

$$\hat{k}_v \approx \frac{1}{2}(\arg(\tilde{\gamma}_{w_v} e^{-i\hat{\phi}}) + 0.8(\pi - 2 \sin^{-1}((\gamma_n^{-1} |\tilde{\gamma}_{w_v}|)^{0.8}))) \quad \gamma_n = \gamma_{snr} \gamma_t \quad - 65$$

Stage 4 : Height estimation

Calculate k_z from baseline geometry and use this to estimate height from k_v as

$$\hat{h}_v = \frac{2\hat{k}_v}{k_z} \quad - 66$$

Stage 5 : Calculate Coherence for arbitrary user selected polarization \underline{w}

Select an arbitrary polarization scattering mechanism \underline{w} for imaging. For each pixel of the image calculate the complex coherence in this channel as shown in 67

$$\begin{aligned} \underline{w} &= \begin{bmatrix} w_1 \\ w_2 \\ w_3 \end{bmatrix} = \begin{bmatrix} \cos \alpha \\ \sin \alpha \cos \beta e^{i\xi} \\ \sin \alpha \sin \beta e^{i\psi} \end{bmatrix} \\ \Rightarrow \begin{cases} s_1 = w_a (S_{HH}^1 + S_{VV}^1) + w_b (S_{HH}^1 - S_{VV}^1) + w_c (S_{HV}^1 + S_{VH}^1) \\ s_2 = w_a (S_{HH}^2 + S_{VV}^2) + w_b (S_{HH}^2 - S_{VV}^2) + w_c (S_{HV}^2 + S_{VH}^2) \end{cases} & - 67 \\ \Rightarrow \tilde{\gamma}(\underline{w}) &= \frac{\langle s_1 s_2^* \rangle}{\sqrt{\langle s_1 s_1^* \rangle \langle s_2 s_2^* \rangle}} \end{aligned}$$

Stage 6 : Calculate Legendre Spectrum for polarization \underline{w}

Now calculate the two Legendre coefficients a_{10} , a_{20} for \underline{w} as shown 68, again using correction factors for SNR and temporal decorrelation effects (if available)

$$\begin{aligned} \tilde{\gamma}_k &= \tilde{\gamma}(\underline{w}) e^{-i(\hat{k}_v + \hat{\phi}_0)} \\ \Rightarrow \hat{a}_{10}(\underline{w}) &= \gamma_n^{-1} \frac{\text{Im}(\tilde{\gamma}_k)}{f_1} \quad \hat{a}_{20}(\underline{w}) = \gamma_n^{-1} \frac{\text{Re}(\tilde{\gamma}_k)}{f_2} - \frac{f_0}{f_2} \quad \gamma_n = \gamma_{snr} \gamma_t \quad - 68 \end{aligned}$$

Stage 7 : Reconstruct normalised vertical profile

Use the two Legendre coefficients and knowledge of the height for each pixel to reconstruct a normalised (to have unit integral) vertical profile of scattering as shown in equation 69

$$\hat{f}_{L2}(\underline{w}, z) = \frac{1}{\hat{h}_v} (1 - \hat{a}_{10}(\underline{w}) + \hat{a}_{20}(\underline{w}) + \frac{2z}{\hat{h}_v} (\hat{a}_{10}(\underline{w}) - 3\hat{a}_{20}(\underline{w})) + \hat{a}_{20}(\underline{w}) \frac{6z^2}{\hat{h}_v^2}) \quad 0 \leq z \leq \hat{h}_v$$

- 69)

In case of strong temporal effects, a_{20} may saturate this reconstruction. In this case use a lower resolution, but more robust first order reconstruction as shown in 70

$$\hat{f}_{L1}(\underline{w}, z) = \frac{1}{\hat{h}_v} ((1 - \hat{a}_{10}(\underline{w})) + \frac{2\hat{a}_{10}(\underline{w})}{\hat{h}_v} z) \quad 0 \leq z \leq \hat{h}_v$$

- 70)

1.6 Case Study : PCT from L-band POLInSAR Simulations

We now turn to consider a worked example of PCT processing. We select the same L band simulations employed in the POLInSAR tutorial and described in [<http://earth.esa.int/polsarpro/tutorial.html>]. To briefly summarise, we consider a 100 x 100m flat scene with a 10m vegetation layer in the centre. This layer is composed of a uniform random volume of branches with sizes distributed according to a Gaussian distribution. The L-band coherent quadpol scattering from such a scene is then simulated using system parameters closely matched to those of the airborne E-SAR system operated by DLR in Germany [13]. This simulation is then repeated for a 10m horizontal offset baseline, so enabling simulation of fully polarimetric interferometry. In the POLInSAR tutorial provided as part of POLSARPro, this simulation was used to demonstrate height and topography retrieval. Here we use the same data set to reconstruct a 3-D image of the scene in different polarizations.

The starting point is to consider estimation of the surface phase ϕ_0 and the normalised wavenumber k_v . The techniques to do this are dealt with in the POLInSAR tutorial and so here we demonstrate the new aspects, namely the use of the phase optimisation algorithm for ϕ_0 estimation.

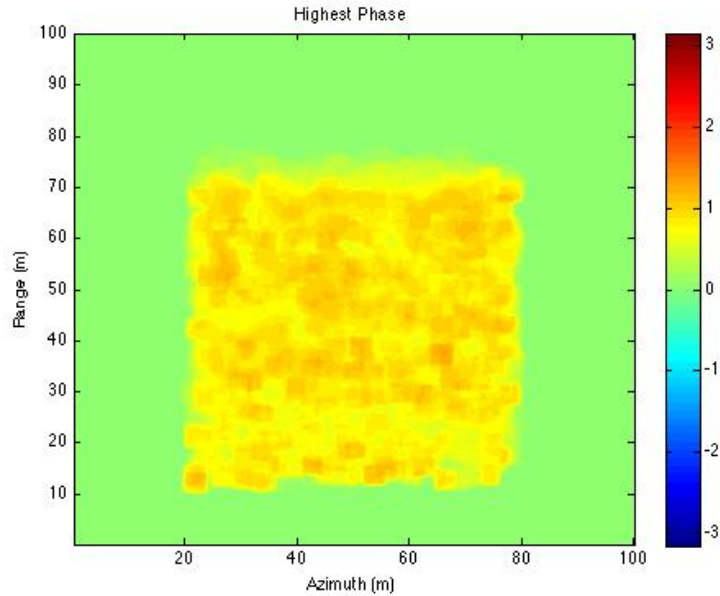


Figure 24 : Interferometric Phase of Polarization with Highest Phase Centre (obtained by phase optimisation)

Figure 24 shows the average phase of the polarization with the highest phase centre in the canopy (using an 11 x 11 averaging window). Note that the true surface phase is everywhere zero and so we can see the effect of the vegetation in providing a phase bias. In contrast, we show in figure 25 the corresponding phase for the polarization with lowest phase centre. We note the much reduced phase bias but can still see the vegetation layer as an increase in mean phase. Note the bias has a minimum some distance into the front of the canopy. This is due to the strong double bounce dihedral return present in this data. The phase centre for this is on the surface and hence the phase optimiser can find a polarization that enhances this return and gives a phase close to the true surface. Elsewhere however we see a residual phase bias.

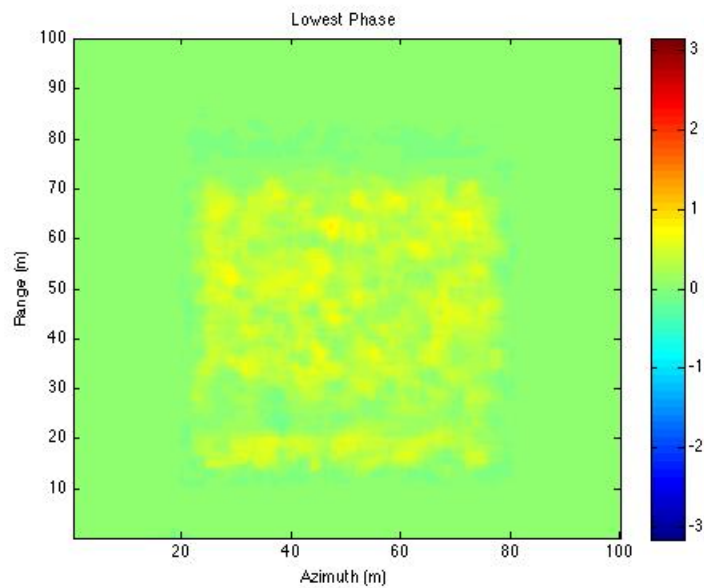


Figure 25: Interferometric Phase of Polarization with Lowest Phase Centre (obtained by phase optimisation)

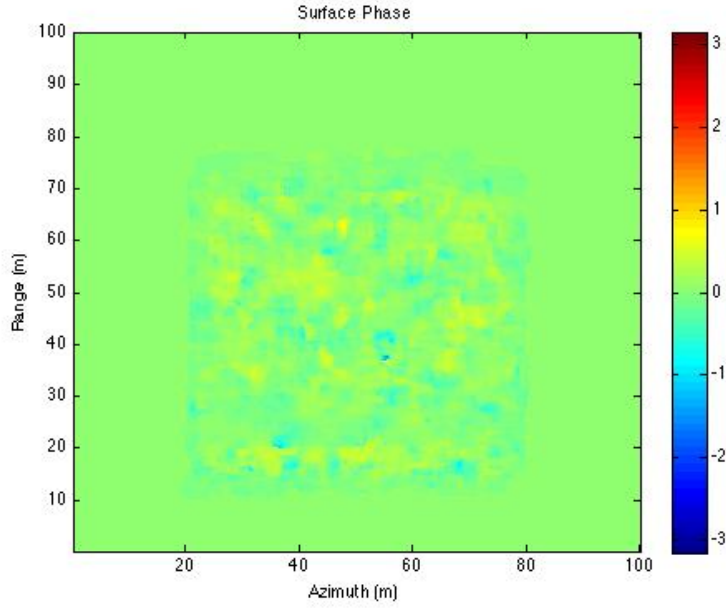


Figure 26: Surface Phase Estimate based on Line fit between the high and low phase centres of figures 24 and 25.

This bias can be further reduced by using the line fit between the high and low phase centres of figures 24 and 25. The resulting ϕ_0 estimate is shown in figure 26. Here we see a further reduction in bias with a residual noise about the correct mean value of zero. This phase image will then provide one of the two parameters required for PCT, namely ϕ_0 . The second, k_v requires a height estimate. This we can obtain by using the high phase centre, together with ϕ_0 in equation 65 (setting $\gamma_{\text{snr}}\gamma_t = 1$). The 10m baseline used here corresponds to $k_z = 0.128$ and hence k_v should have two values, $k_v = 0$ outside of the canopy (where the height is zero) and $k_v = 0.641$ inside the canopy. Figure 27 shows the results obtained using equation 65.

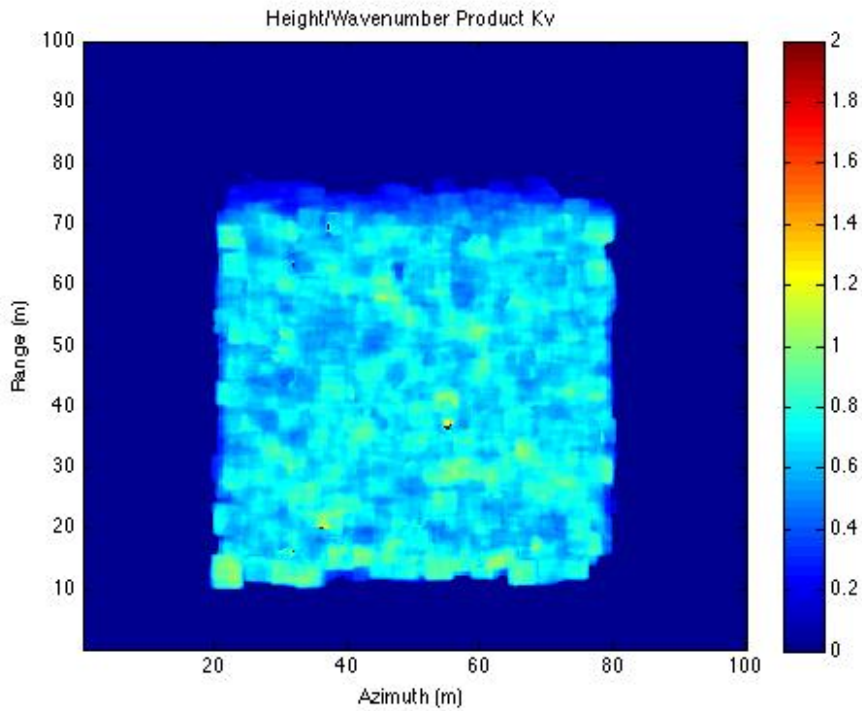


Figure 27 : Estimate of normalised baseline k_v

We note three regions of interest. In the non-vegetated areas we obtain $k_v = 0$ as expected. In the main canopy we obtain a spread of values around some mean value except for the very far range where we see a thin band of lower k_v values. This is the taper into the shadow region where the effective volume component for that slant range is reduced due to the layover distortion effect and hence the effective volume height reduces. Figure 28 shows a histogram of the k_v estimates over the nonzero regions of figure 27. Also shown as a dashed line is the true k_v value. We see the low plateau caused by the far range shadow region but see a main peaked distribution with a mean close but slightly higher than the true value. The peak of the histogram occurs at $k_v = 0.66$, giving an overestimation of around 3% in k_v . In order to track the effect of these errors (and also those in the surface phase) in what follows we compare the PCT parameters obtained using POLInSAR (called the estimated parameter set) against those based on the known values (called the true parameter set). For example, we can use the known k_v to calculate the triplet of Legendre coherence function values f_0 , f_1 and f_2 as shown in equation 71

$$k_v = 0.641 \Rightarrow f_0 = 0.933, f_1 = 0.205, f_2 = -0.027 \quad - 71)$$

These can now be calculated from the estimated k_v values of figure 27. We show histograms of the estimates in figure 29. Again we see three peaked distributions around the correct values (shown as dashed lines). Note again the small plateau features caused by the shadow region.

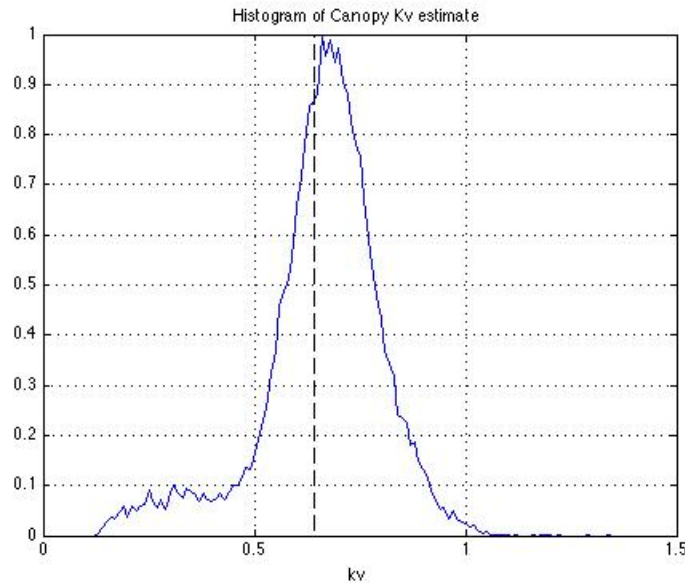


Figure 28: Histogram of estimated k_v values for the canopy region of figure 27

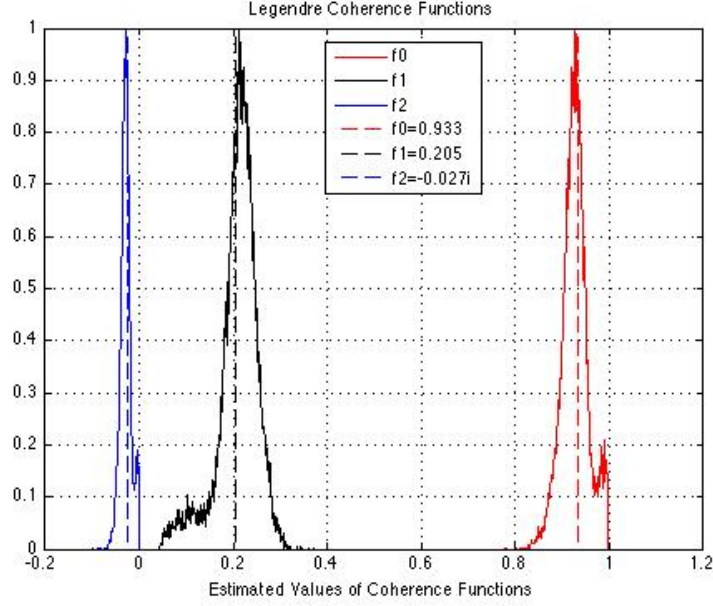


Figure 29: Histograms of estimates of the Legendre functions f_0 , f_1 and f_2 used in PCT

Now we have obtained estimates for all the polarization independent parameters require for PCT, namely ϕ_0 , k_v and the triplet of Legendre function f_0 , f_1 and f_2 , we can turn to consider the use of these for estimation of the Legendre spectrum for a given polarization channel.

1.6.1 Estimation of the Legendre Spectrum for arbitrary polarization w

We now turn to consider the first stage in constructing a 3-D image of the scene, namely estimation of the unknown coefficients of the Legendre series. As we have access to only single baseline data, we can estimate two of these for each pixel, a_{10} and a_{20} (with a_{00} set to 1 by convention). One problem for validation, even when we use the true parameter set, is that we do not know what these coefficients should be for this scene. Nonetheless, we know that one major source of uncertainty will come from estimation of the complex coherence itself. This is a stochastic quantity with well characterised but nontrivial fluctuation statistics and the first thing we need to secure is an appropriate window size to make sure we have no coherence bias effects in the estimation. To confirm this we show in figure 30 two histograms of the estimate of a_{10} on the left and a_{20} on the right (from equation 68 and using the true parameter set in the HV polarization channel)

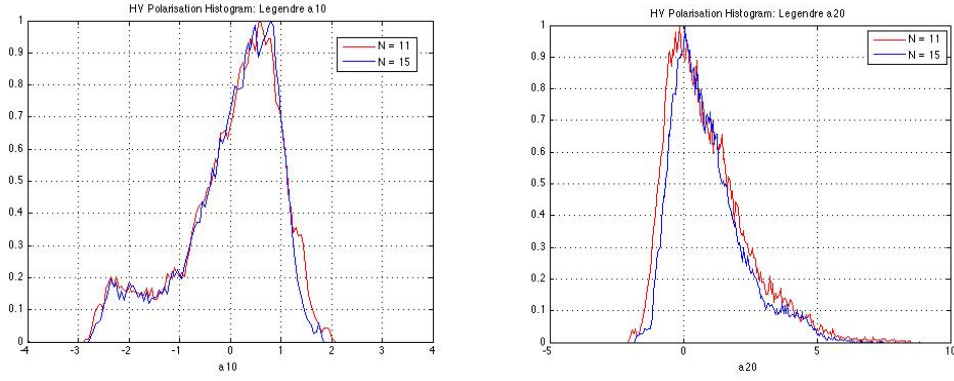


Figure 30 : Histograms of estimates of a_{10} (left) and a_{20} (right) for $N = 11$ and 15 coherence estimation window sizes

In both cases we show a reference set (in red) for an 11×11 averaging window and in blue the corresponding estimates obtained for a larger window of 15×15 . We see little difference between the estimates suggesting that our proposed 11×11 window is already enough to remove any significant estimation bias. Considering the a_{10} results, again we see a plateau due to the shadow region but, concentrating on the main distribution, we see a peak around $a_{10} = +0.75$. This corresponds to a vertical profile that reduces with depth into the canopy, as expected for the cross-polarized channel, where there will be small surface contributions. The a_{20} results show a different distribution. Here we see a peak around $a_{20} = 0$, but a wider spread of estimates in positive a_{20} than in negative. This reflects the asymmetric distributions of the two regions in the coherence plane of figure 16.

The next stage is to determine how sensitive these parameters are to changes in polarization. In figure 31 we show comparative histograms of a_{10} (upper) and a_{20} (lower) for the canopy region for three different polarizations (using the true parameter set). In black we show for reference the cross-polarized HV channel. In red and blue we show the results for the two phase optima identified in figures 24 and 25. Here we see large differences in the structure function between polarizations. The surface dominated (minimum phase bias) channel \underline{w}_s shows very small (negative) a_{10} and high (positive) a_{20} values, indicating a structure function localised around $z = 0$ i.e. near the surface. In contrast the volume dominated (maximum phase bias) channel \underline{w}_v shows high positive a_{10} and low positive a_{20} , indicating a structure function near the top of the canopy with only a small residual surface component. We note that a_{20} always has a noisier histogram than a_{10} , reflecting its increased sensitivity to fluctuations in coherence.

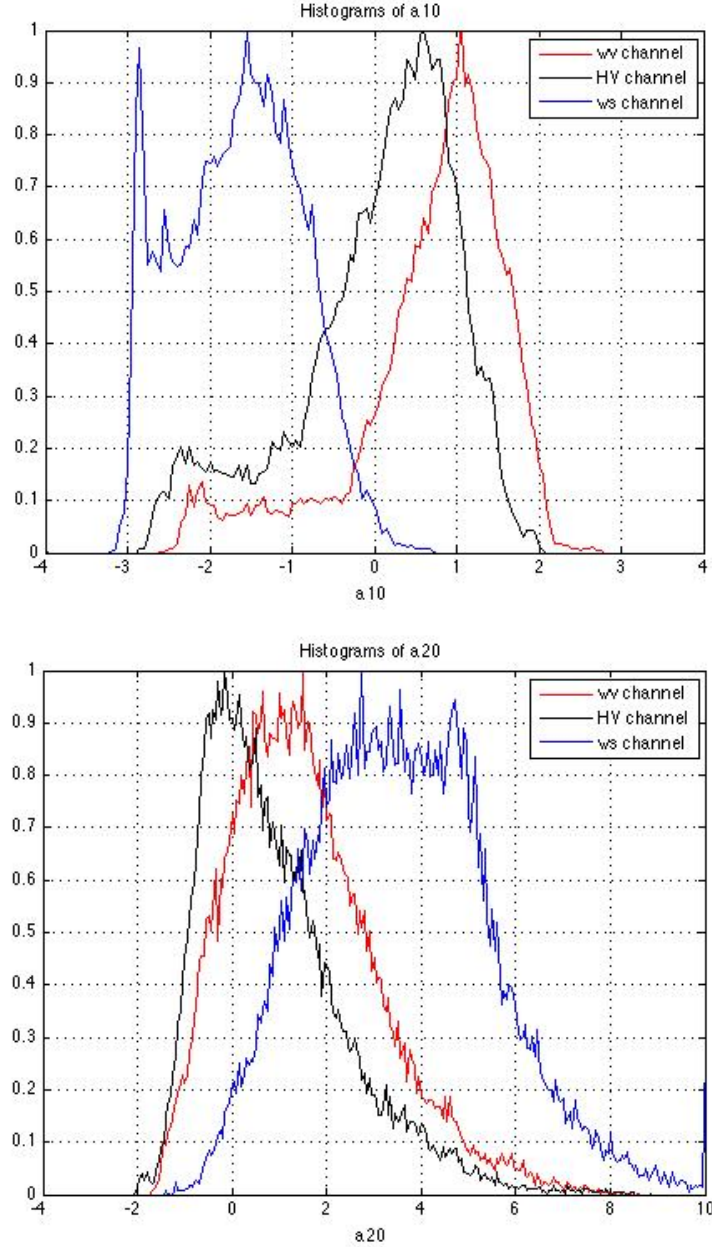


Figure 31: Histograms of a_{10} (upper) and a_{20} (lower) using the true parameter set for 3 different polarizations, HV in black and the two phase optima, the volume dominated channel \underline{v}_v in red and the surface dominated channel \underline{v}_s in blue.

The key issue we now want to resolve is how do these Legendre estimates change when we no longer have access to the true parameter set and have to employ instead estimates of ϕ_0 and k_v . Figure 32 summarises the results, again in the form of histograms over the canopy region. Turning first to the results for a_{10} , we see that while there is still good separation of structures with polarization, the quantitative estimates have changed. In general the values are lower than those obtained using the true parameter set in figure 31. This tends to overestimate contributions to the structure function from deeper in the volume. The results for a_{20} show some very different behaviour. The key feature here is the cut-off for negative a_{20} in the volume channel. This arises from the approximation employed in equation 63 and traced to the behaviour in figure 21. The use of $\varepsilon = 0.8$ amounts to assuming that $a_{20}=0$ in the

volume dominated channel and hence precludes negative a_{20} estimates for this special channel. Note however that the estimates of a_{20} in the other channels remain similar to the original set in figure 31, although the surface component now has a narrower distribution. We now turn finally to consider the implications of these effects for 3-D imaging of the canopy.

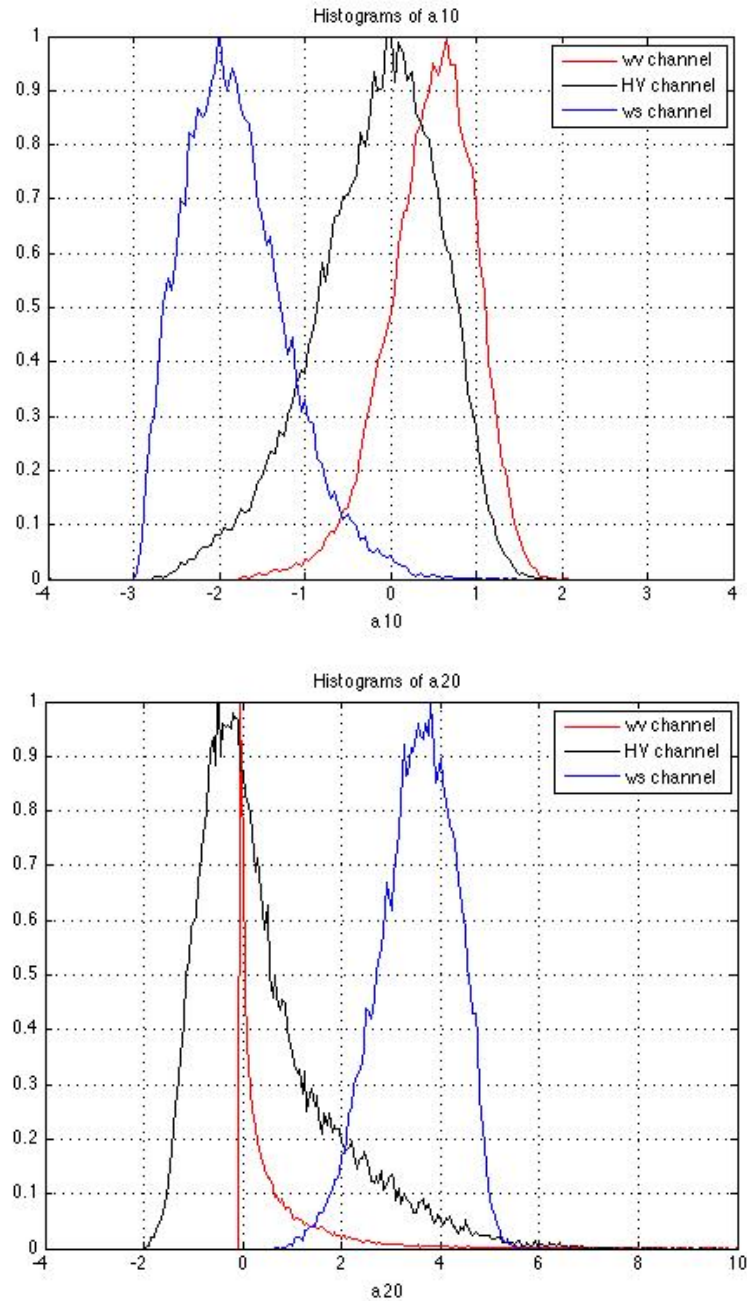


Figure 32: Histograms of a_{10} (upper) and a_{20} (lower) using the estimated parameter set for 3 different polarizations, HV in black and the two phase optima, the volume dominated channel \underline{w}_v in red and the surface dominated channel \underline{w}_s in blue.

1.6.2 3-D Imaging Results

In the previous section we looked at histograms over the canopy of estimates of the Legendre parameters a_{10} and a_{20} . Here we extend this analysis to look more closely at the spatial variation of these parameters and at their use in generating 3-D images of the scene.

We could choose to look at arbitrary polarizations states \underline{w} , but as important examples concentrate on the copolarised HH and crosspolarised HV channels. These are commonly used in low frequency (L and P band) systems for forest and vegetation mapping applications. Figure 33 shows images of the a_{10} Legendre parameter estimates using the estimated height and topographic phase in the upper part and the true parameter set (known height of 10m and known surface phase of zero) in the lower. This enables us to compare spatial differences in the estimates.

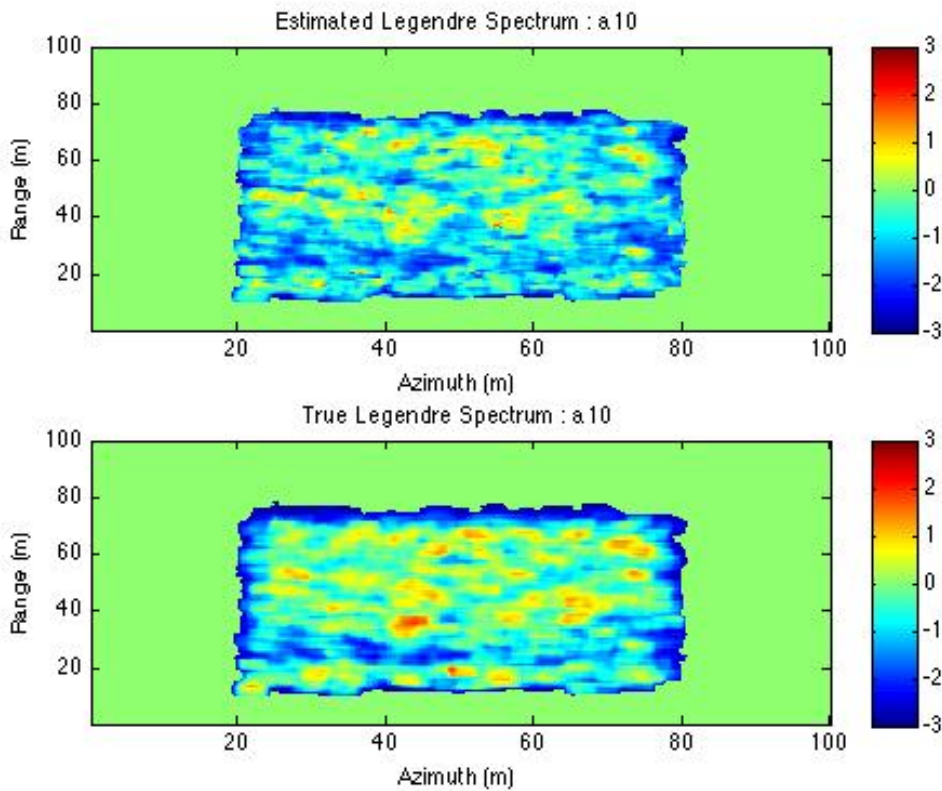


Figure 33: Image of a_{10} Legendre estimate for HH Polarization using estimated parameters (upper) and known parameters (lower)

We note that there is a band near the front of the canopy with a low negative (blue) value. This corresponds to a region with strong surface scattering compared to the region further in range when the parameter changes sign (yellow) indicating more attenuation of the HH response. Importantly we see this behaviour repeated in both the true and estimated parameter sets, although the range of values is compressed slightly in the estimated set. Figure 34 shows the corresponding images for the crosspolarized or HV channel. We again note the difference between near and far range, but here note a more positive a_{10} parameter, indicating reduced surface scattering, as expected in this channel

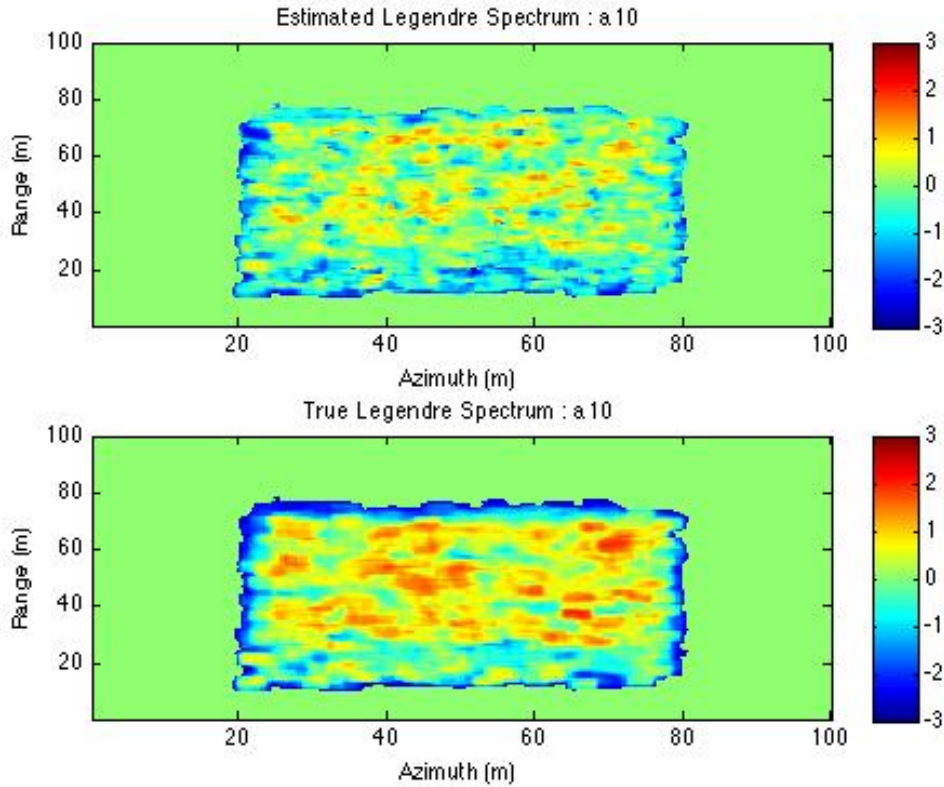


Figure 34: Image of a_{10} Legendre estimate for HV Polarization using estimated parameters (upper) and known parameters (lower)

Figures 35 and 36 show the corresponding images of the second order a_{20} parameter, again showing results for both the estimated and true parameter sets. In HH we see again a band in near range where the parameter is large and positive, indicating a strong surface contribution. In the far range there are still some positive regions but others show a change of sign, indicating again a reduction of the apparent surface return. In the crosspolarized HV channel we see very different behaviour. Here it is negative (blue) across large parts of the canopy. This again supports our understanding of the physics of scattering in the crosspolarised channel, which will have a reduced surface component and hence a vertical structure function concentrated near the top of the canopy.

We can now use the Legendre parameters a_{10} and a_{20} to reconstruct the vertical structure function for each pixel in the image. In this way we obtain a 3-D image, PCT providing the z variation for each xy pixel of the SAR image. To demonstrate this idea we select an azimuth cut across the image and visualise the variation of structure function. Figures 37 and 38 show sample results for HH and HV polarizations respectively. Again for each polarization we show two different estimates. In the upper case we show the structure function estimate obtained for the true height and surface phase. In the lower part the structure function obtained from the estimated height and phase. In the HH channel we see a structure function concentrated near the surface (this slice is taken near the front of the canopy at range bin 71). This basic shape is maintained in the estimated reconstruction as well, although there is more fluctuation due to the height and topography errors.

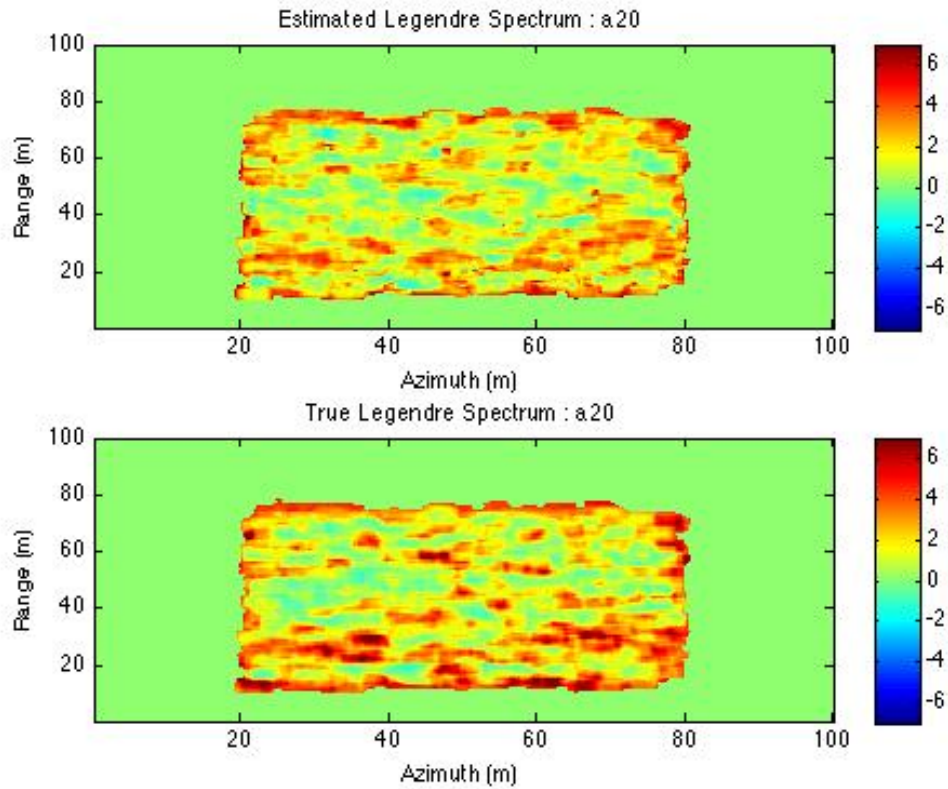


Figure 35: Image of a_{20} Legendre estimate for HH Polarization using estimated parameters (upper) and known parameters (lower)

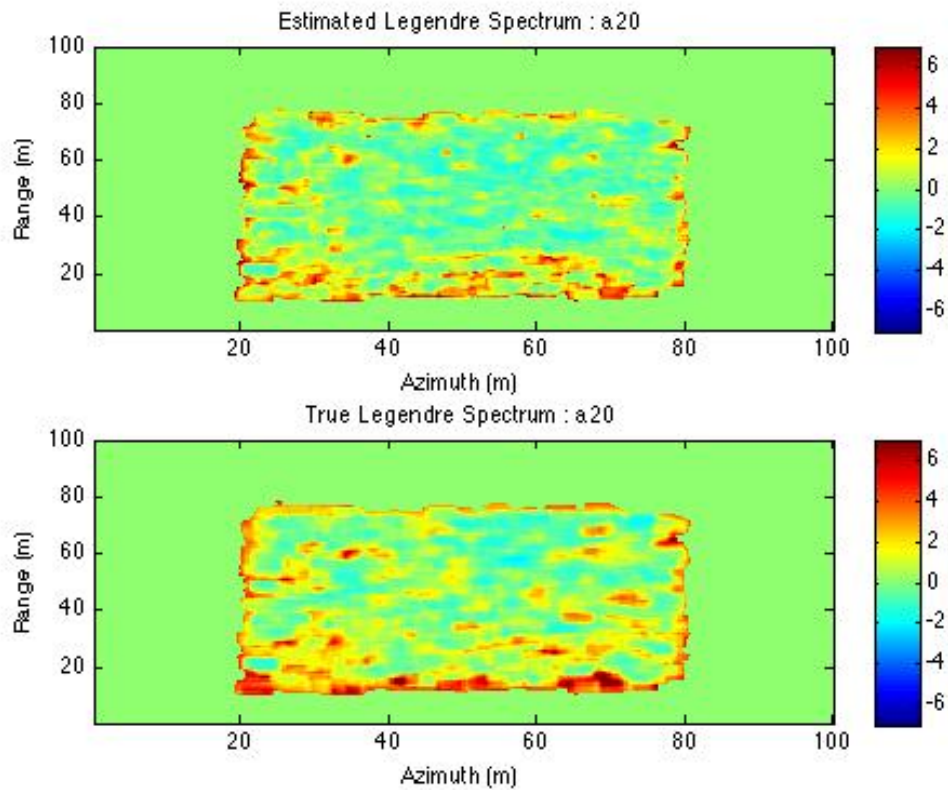


Figure 36: Image of a_{20} Legendre estimate for HV Polarization using estimated parameters (upper) and known parameters (lower)

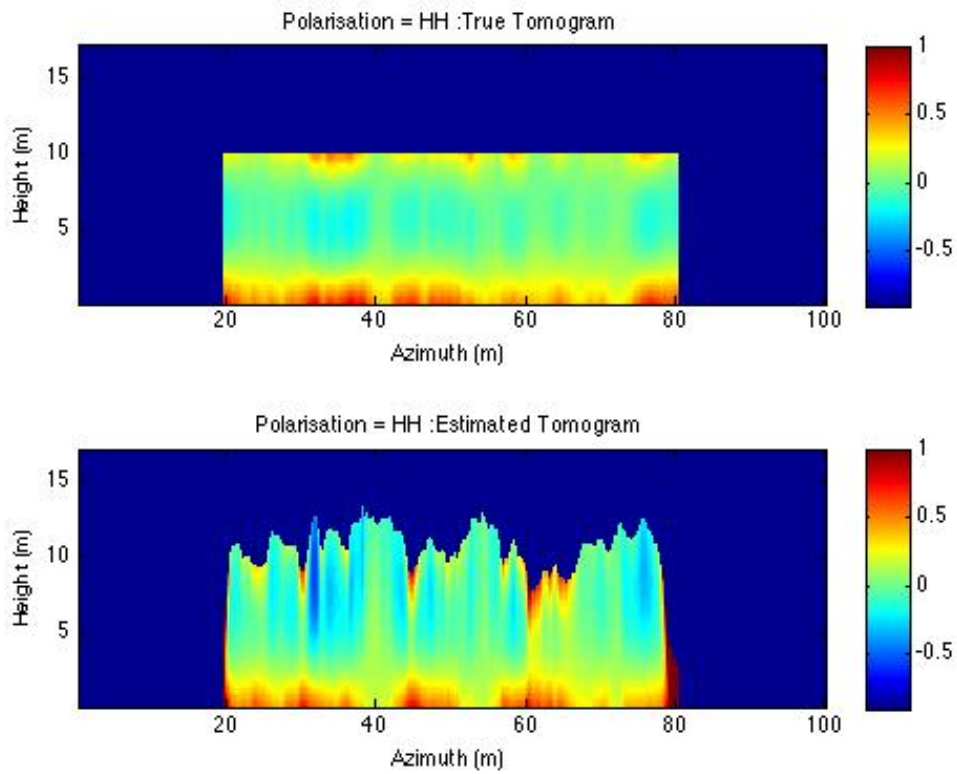


Figure 37: Azimuth slice through canopy (using row 71 of data set) for HH Polarization using known parameters (upper) and estimated parameters (lower)

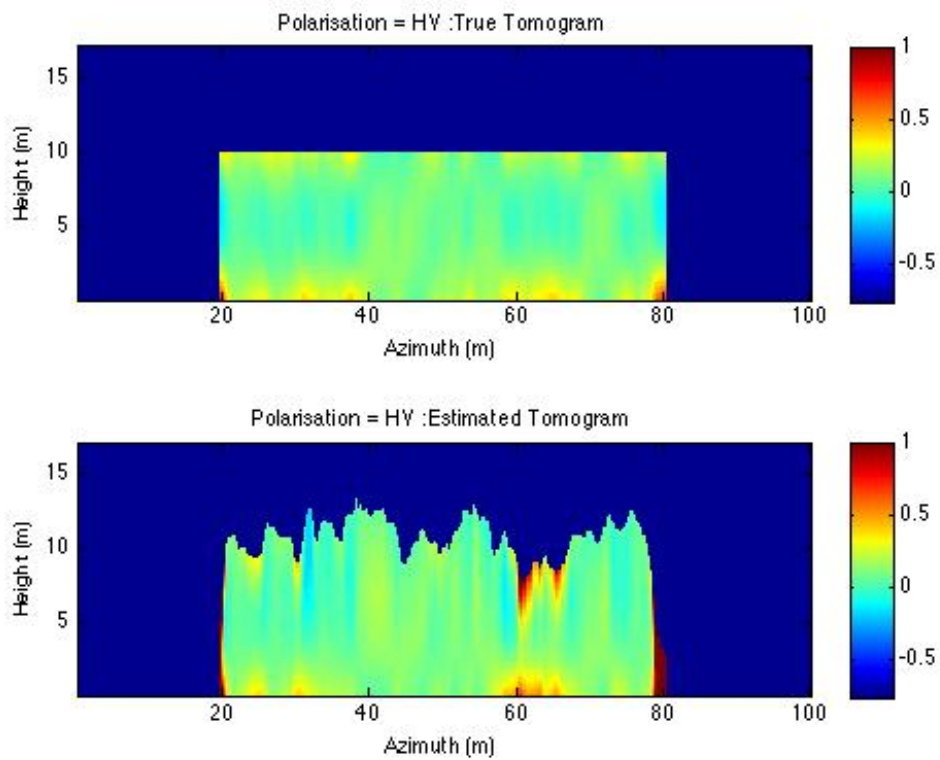


Figure 38: Azimuth slice through canopy (using row 71 of data set) for HV Polarization using known parameters (upper) and estimated parameters (lower)

Figure 38 shows the results for the same azimuth slice but in the HV polarization channel. Here we see less (but not zero) surface component and a more uniform volume response. Again this same basic pattern is seen in the estimated data. If we move further out in range then the structure function changes, as expected from the Legendre parameter images. As an example we show in figure 39 a slice at range 141 in the data set for the HH polarization. Compared to figure 37 we now see a reduced surface component. Again this reduction is mirrored in the estimated tomogram.

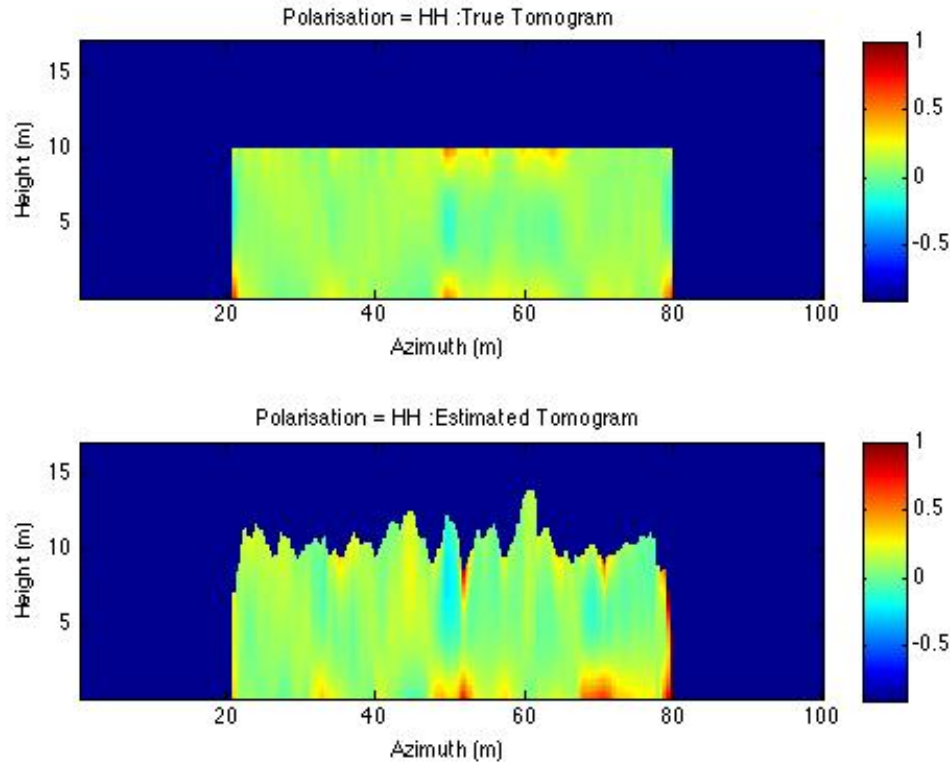


Figure 39: Azimuth slice through canopy (using row 141 of data set) for HH Polarization using known parameters (upper) and estimated parameters (lower)

This begs the question as to whether there are any polarizations with a stronger surface component than HH. To answer this and demonstrate the ability of PCT to map arbitrary polarizations, we show in figure 40 a cut through the 3-D image for the same azimuth slice as in figure 39 (row 141) but for the optimum polarization channel that always maximises the surface component in the structure function. Here we see a much stronger surface component than that found in HH. This highlights the difference between Quadpol systems, which provide user access to all polarizations and those that use fixed polarizations, such as HH and HV. The former allow access to much better separation of surface and volume scattering and hence to a much wider range of vertical structure functions.

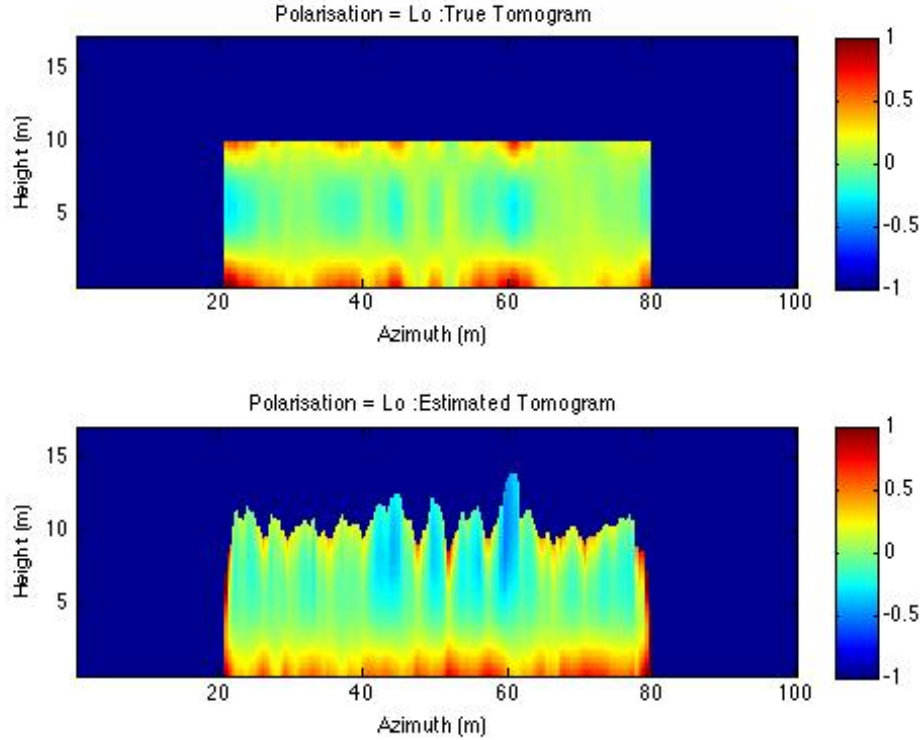


Figure 40: Azimuth slice through canopy (using row 141 of data set) for Optimum Surface Polarization using known parameters (upper) and estimated parameters (lower)

1.7 Conclusions

In this tutorial we have introduced the idea of using interferometric coherence for 3-D radar imaging. The main technique developed, called polarization coherence tomography or PCT, involves first using the variation of interferometric phase centre with polarization to estimate two bounding parameters for each pixel in a SAR image, namely the surface topographic phase and top height of the layer. These two are then employed with the complex coherence for arbitrary polarization to secure estimates of two terms of the Fourier-Legendre series expansion of the unknown vertical structure function at each pixel. These parameters can then be used to reconstruct a quadratic approximation to the structure function and hence a 3-D image of the scene.

We have shown that to implement PCT we need to make two assumptions about the scattering medium, namely that the volume scattering component is random (has azimuthal symmetry) and secondly that we can always find at least one polarization with a volume dominated response and a structure function that decays with depth into the volume. However PCT no longer requires the assumption of a fixed exponential structure function, as widely used for example in the RVOG model. This gives it more flexibility to describe a wider range of vertical profiles.

We have illustrated application of the technique to simulated L-band data for a simple scene comprising a 10m vegetation layer surrounded by a bare surface. This scene is the same as that employed in the POLInSAR tutorial. We have used this example to generate 3-D images for various polarization channels and to illustrate issues relating to the effects of window size and uncertainties in height and topography estimation.

1.8 References

- [1] R.N. Treuhaft, B. E. Law, G. P. Asner, "Structural Approaches to Biomass Monitoring with Multibaseline, Multifrequency, Polarimetric Interferometry", *Proceedings of 3rd European SAR Conference (EUSAR)*, Munich, Germany, pp 253-255, May 2000
- [2] R.N. Treuhaft, G.P. Asner, B.E. Law, S. Van Tuyl, "Forest Leaf Area Density Profiles from the Quantitative Fusion of Radar and Hyperspectral data", *J. Geophys. Res.*, 107(D21), 4568, 2002
- [3] R.N. Treuhaft, P. Siqueria, "Vertical Structure of Vegetated Land Surfaces from Interferometric and Polarimetric Radar", *Radio Science*, Vol. 35(1), pp 141-177, January 2000
- [4] T. Mette "Forest Biomass Estimation from Polarimetric SAR Interferometry", DLR Research Report 2007-10, ISSN 1434-8454, 2007
- [5] O. Stebler, O., Meier, E., Nuesch, D., "Multi-Baseline Polarimetric SAR Interferometry - first experimental spaceborne and airborne results". *ISPRS Journal of Photogrammetry and Remote Sensing*, 56(3), 2002
- [6] A. Reigber, A. Moreira, "First Demonstration of Airborne SAR Tomography Using Multi-Baseline L-Band Data", *IEEE Transactions on Geoscience and Remote Sensing*, Vol. 38/5, pp 2142-2152, September 2000
- [7] A. Reigber, K.P. Papathanassiou, S. Cloude, A. Moreira, "SAR Tomography and Interferometry for the Remote Sensing of Forested Terrain", *Frequenz*, 55,, pp 119-123, March/April 2001
- [8] G. Fornaro, F. Serafino, F. Soldovieri "Three Dimensional Focusing with Multipass SAR Data", *IEEE Transactions, Geoscience and Remote Sensing*, vol. 41, Mar, 2003, pp 507-517
- [9] S R Cloude, "Polarization Coherence Tomography", *Proceedings of 6th European SAR Conference*, EUSAR 06, Dresden, May 2006
- [10] S. R. Cloude, "Polarization Coherence Tomography", *Radio Science*, 41, RS4017, September 2006
- [11] S R Cloude, "Dual Baseline Coherence Tomography", *IEEE Geoscience and Remote Sensing Letters*, Vol4, No. 1, January 2007, pp 127-131
- [12] S.R Cloude, K P Papathanassiou, "Polarimetric SAR Interferometry", *IEEE Transactions on Geoscience and Remote Sensing*, Vol 36. No. 5, pp 1551-1565, September 1998
- [13] K.P. Papathanassiou, S.R. Cloude, "Single Baseline Polarimetric SAR Interferometry", *IEEE Transactions Geoscience and Remote Sensing*, Vol 39/11, pp 2352-2363, November 2001
- [14] S.R. Cloude, K.P. Papathanassiou, "A 3-Stage Inversion Process for Polarimetric SAR Interferometry", *IEE Proceedings, Radar, Sonar and Navigation*, Volume 150, Issue 03, June 2003, pp 125-134
- [15] G Krieger, K P Papathanassiou, S R Cloude, "Spaceborne Polarimetric SAR Interferometry: Performance Analysis and Mission Concepts", *EURASIP Journal of Applied Signal Processing*, Vol. 20, pp 3272-3292, 2005
- [16] S.R. Cloude, E. Pottier, "An Entropy Based Classification Scheme for Land Applications of Polarimetric SAR", *IEEE Transactions on Geoscience and Remote Sensing*, Vol. 35, No. 1, pp 68-78, January 1997
- [17] E. Colin, C Titin-Schneider, W Tabbara, "Investigation of Different Interferometric Coherence Optimisation Methods", *Proceedings of 1st ESA Workshop on Applications of SAR Polarimetry and Polarimetric Interferometry (POLInSAR 03)*, January 2003, SP-529, <http://earth.esa.int/workshops/polinsar2003/>
- [18] E. Colin, Titin-Schneider, C.; Tabbara, W, "An interferometric coherence optimization method in radar polarimetry for high-resolution imagery." *Geoscience and Remote Sensing, IEEE Transactions on*, Volume 44, Issue 1, Jan. 2006 Page(s):167 – 175
- [19] M. Tabb, J Orrey, T Flynn, R Carande, "Phase Diversity: A Decomposition for Vegetation Parameter Estimation using Polarimetric SAR Interferometry", *Proceedings of 4th European Synthetic Aperture Radar Conference*, EUSAR 2002, pp 721-724
- [20] T Flynn, Tabb M., Carande R., "Coherence Region Shape Estimation for Vegetation Parameter Estimation in POLINSAR", *Proceedings of IGARSS 2002*, Toronto, Canada, pp V 2596-2598